Reduction of the Auger rate in semiconductor quantum dots

Janet L. Pan
Research Laboratory of Electronics, Room 38-290, Massachusetts Institute of Technology, Cambridge, Massachusetts 02139
(Received 2 October 1991; revised manuscript received 11 February 1992)

We propose the use of quantum dots in semiconductor lasers to reduce the Auger rate, the dominant process limiting the performance of today's semiconductor lasers in the thermal infrared. We will see that many Auger processes cannot occur in quantum dots that are surrounded by a very large potential energy barrier because continuum energy states are not available as final states. We present many possible materials that can be used for these quantum dots and barriers. We also derive an analytical expression for the Auger rate in a quantum sphere, in which there are two electrons and two holes, in terms of Slater integrals, reduced matrix elements, and Racah coefficients of total-angular-momentum quantum numbers. We note that the total angular momentum must be conserved for Auger processes in a quantum dot, unlike the linear momentum conservation law required in the bulk. We present a practical example of a 150-Å-radius InSb quantum dot surrounded by CdTe barriers, whose room-temperature band gap is at 4.8 μm (258 meV), and whose room-temperature Auger lifetime is calculated as 135 ns, which is at least two orders of magnitude better than the Auger lifetime in other *low-temperature* semiconductor lasers. We present partial Auger rates and tabulate them in a Grotrian diagram labeled by the bound states involved. We calculate and discuss the temperature dependence of quantum-dot Auger rates. In calculating the (nonparabolic) band structure and energy states, we use a multiband envelope-function approximation in eight-band $\mathbf{k}\cdot\mathbf{p}$ theory, which also included some of the effects of higher-order bands. Single and multiparticle eigenstates are chosen to diagonalize the total angular momentum. We include valence-band mixing in calculating our single-particle quantum-dot states.

I. INTRODUCTION

The Auger rate is the dominant[1,2] process limiting the performance of today's semiconductor lasers in the thermal infrared, whose wavelengths are between 2 and 10 μm. Lasers in this wavelength regime, such as the lead salt lasers, are already being used in spectroscopy because many substances have characteristic spectra in the thermal infrared. A room-temperature semiconductor laser in this wavelength range (greater than 2 μm) would also be of great importance in optical fiber communication, where many substances, such as fluoride fibers, silver halide fibers,[3,4] chalcogenide and pnictide fibers,[5,6] have theoretical intrinsic losses that are one or two orders of magnitude lower than those of currently used silica fibers.

Recently, Auger processes have been proposed[7] as an important nonradiative-recombination mechanism which explains experimental data in semiconductor microcrystals grown in oxide glass. In this paper, we consider the possibility of using quantum dots that are surrounded by materials forming a very large potential energy barrier to reduce the Auger rate for a semiconductor quantum-dot laser. We will see below that in the presence of these potential barriers, many Auger processes cannot occur because continuum final-energy states are not available, especially for those processes involving initial electrons and holes close to the band extrema. While quantum dots have already been proposed for semiconductor lasers as a method of increasing laser efficiency[8] because their density of states can be made more peaked at the desired frequency than that in the bulk, we propose the use of large potential barriers with quantum dots as a way of reducing the Auger rate. In Sec. III, we present possible materials that can be used for these quantum dots and barriers.

In order to make contact with the notation and results in the literature, we review the general expression for the Auger rate in Sec. II. We shall see that the confinement in all three dimensions in a quantum "box" necessitates a different form for the integrals to be evaluated. In a particular case where closed-form solutions are available, the spherical symmetry of a quantum sphere allows the eigenstates to be simultaneously those of energy and total angular momentum, as discussed in Sec. IV A. An analytical expression for the Auger rate and its selection rules in a quantum dot are derived in Sec. IV B. In Sec. V, we present a practical example of an InSb quantum dot in which the Auger rate is substantially reduced with respect to that in the bulk. We also calculate and discuss the temperature dependence of the Auger rate. We conclude with a summary in Sec. VI.

II. THE GENERAL EXPRESSION FOR THE AUGER RATE

In this section, we present equations that are used to calculate the Auger rate in general. We do this not only to summarize some well-known important points, but also to contrast those issues that may change as we go from the three-dimensional bulk to the zero-dimensional quantum dot. We will review conservation of linear momentum for bulk Auger processes. We will note that the Coulomb interaction is taken between the envelope

and not the Bloch lattice periodic parts of the wave functions. Finally, in Sec. II B, we sketch a general method for calculating Auger rates in the presence of more complicated geometries and with more sophisticated wave functions.

Fermi's golden rule gives the Auger rate as[2,3,9]

$$R_A=\frac{2\pi}{\hbar}\frac{1}{N_{\text{initial}}}\sum_{\text{initial states}}\sum_{\text{final states}}|V_{if}|^2\delta(E_i-E_f)\ , \quad (1)$$

where N_{initial} is the number of initial states, and where V_{if} is the matrix element of the Coulomb interaction between the participating electrons; and E_i and E_f are the total initial and total final energies for the Auger process. The Auger processes result from the Coulomb interaction between the electrons. Thus, the interaction potential V taken between two electrons is

$$V(\mathbf{r}_1-\mathbf{r}_2)=\frac{q^2}{4\pi\epsilon|\mathbf{r}_1-\mathbf{r}_2|}\exp(-\lambda|\mathbf{r}_1-\mathbf{r}_2|)\ , \quad (2)$$

where $\mathbf{r}_1$ and $\mathbf{r}_2$ are the positions of the two electrons, ϵ is the dielectric constant, and λ is the inverse screening length. The initial- and final-state wave functions to be used in the matrix element in (1) are Slater determinantal in the N_{elec} single-particle wave functions, $\Phi_i(\tau_j)$,

$$\frac{1}{\sqrt{N_{\text{elec}}}}\begin{vmatrix}\Phi_1(\tau_1) & \Phi_2(\tau_1) & \cdots & \Phi_{N_{\text{elec}}}(\tau_1)\\ \Phi_1(\tau_2) & \Phi_2(\tau_2) & \cdots & \Phi_{N_{\text{elec}}}(\tau_2)\\ \vdots & \vdots & & \vdots\\ \Phi_1(\tau_{N_{\text{elec}}}) & \Phi_2(\tau_{N_{\text{elec}}}) & \cdots & \Phi_{N_{\text{elec}}}(\tau_{N_{\text{elec}}})\end{vmatrix}\ , \quad (3)$$

where τ represents both spin and spatial coordinates

$$\tau=(\sigma,\mathbf{r}) \quad (4)$$

with σ denoting the up or down nature of the z component of the electron spin. The matrix element of $\sum_{i<j}V(\mathbf{r}_i-\mathbf{r}_j)$ between Slater determinantal initial and final states is often calculated[10] in the literature, especially in atomic physics,

$$V_{if}=\int\int d\tau_1 d\tau_2[\Phi_1^*(\tau_1)\Phi_2^*(\tau_2)-\Phi_1^*(\tau_2)\Phi_2^*(\tau_1)]\times V(\mathbf{r}_1-\mathbf{r}_2)\Phi_1'(\tau_1)\Phi_2'(\tau_2)\ , \quad (5)$$

where Φ_i and Φ_i', $i=1,2$, denote the wave functions of the two initial and final electrons, respectively, involved in an Auger process. Antisymmetric wave functions in combination with angular-momentum recoupling can be very cumbersome for an arbitrary number of electrons and holes and is discussed further[11] in the atomic physics literature.

For Hamiltonians that are *independent of the electron spin,* the electron wave functions are products of a spin function and a spatial function

$$\Phi_i(\tau)=\phi_i(\mathbf{r})\chi_i(\sigma)\ . \quad (6)$$

Equation (5) then reduces to the well-known expression,[2,3]

$$V_{if}=\int\int[\phi_1^*(\mathbf{r}_1)\phi_2^*(\mathbf{r}_2)\Delta_{21}-\phi_2^*(\mathbf{r}_1)\phi_1^*(\mathbf{r}_2)\Delta_{12}]\times V(\mathbf{r}_1-\mathbf{r}_2)\phi_1'(\mathbf{r}_1)\phi_2'(\mathbf{r}_2)d^3\mathbf{r}_1 d^3\mathbf{r}_2\ , \quad (7)$$

with $\Delta_{21}=\Delta_{12}=1$ when the electrons have the same spin; with $\Delta_{21}=1$, $\Delta_{12}=0$ when the transition preserves both electrons' opposite spins; and with $\Delta_{21}=0$, $\Delta_{12}=1$ when the transition flips both electrons' opposite spins.

A. The Auger rate in the bulk

In a bulk semiconductor, the translational symmetry of the lattice and Bloch's theorem allows us to write the electron wave functions as a product of a Bloch function u_i, which has the periodicity of the lattice, and an envelope function, which in this case is a plane wave

$$\phi_n(\mathbf{r})=u_n(\mathbf{k},\mathbf{r})\exp(i\mathbf{k}\cdot\mathbf{r})=\frac{1}{\sqrt{V}}\sum_{\mathbf{G}}A_n(\mathbf{k},\mathbf{G})\exp[i(\mathbf{G}+\mathbf{k})\cdot\mathbf{r}]\ , \quad (8)$$

where $\mathbf{k}$ is a reduced-zone wave vector, and $\mathbf{G}$ is a reciprocal lattice wave vector. This translational symmetry will give rise to the well-known[1,2] conservation of linear momentum rule in bulk Auger processes.

Beattie and Landsberg[9] showed that the Coulomb term in (2) acts only on the envelope and *not* on the lattice periodic Bloch functions u when the wave number associated with the Auger process momentum exchange is a lot smaller than an inverse lattice spacing; this is a consequence of the slowly varying nature, on the scale of a lattice spacing, of the Coulomb potential between the electrons (holes) participating in the Auger process. To show this, we insert (8) in (7). The first integral in (7) becomes, as the inverse screening length λ goes to zero[9] (which is a good approximation as we discuss in Sec. IV B),

$$\int\int\phi_1^*(\mathbf{r}_1)\phi_2^*(\mathbf{r}_2)V(\mathbf{r}_1-\mathbf{r}_2)\phi_1'(\mathbf{r}_1)\phi_2'(\mathbf{r}_2)d^3\mathbf{r}_1 d^3\mathbf{r}_2=\frac{q^2}{\epsilon V}\sum_{\mathbf{G}_1,\mathbf{G}_2,\mathbf{G}_1',\mathbf{G}_2'}A_{n1}^*(\mathbf{k}_1,\mathbf{G}_1)A_{n2}^*(\mathbf{k}_2,\mathbf{G}_2)A_{n1}'(\mathbf{k}_1',\mathbf{G}_1')A_{n2}'(\mathbf{k}_2',\mathbf{G}_2')\times\frac{\delta(\mathbf{G}_1+\mathbf{G}_2-\mathbf{G}_1'-\mathbf{G}_2'+\mathbf{k}_1+\mathbf{k}_2-\mathbf{k}_1'-\mathbf{k}_2')}{|\mathbf{G}_1-\mathbf{G}_1'+\mathbf{k}_1-\mathbf{k}_1'|^2}\ . \quad (9)$$

When the wave number associated with the Auger process momentum exchange $\mathbf{k}_1-\mathbf{k}_1'$ is a lot smaller than an inverse lattice spacing, as is the case for Auger processes involving energy exchanges on the order of an eV or less,[9] then the dominant terms in (9) are those with $\mathbf{G}_1=\mathbf{G}_1'$ and $\mathbf{G}_2=\mathbf{G}_2'$. Equation (9) then simplifies to[9]

$$\int\int \phi_1^*(\mathbf{r}_1)\phi_2^*(\mathbf{r}_2)V(\mathbf{r}_1-\mathbf{r}_2)\phi_1'(\mathbf{r}_1)\phi_2'(\mathbf{r}_2)d^3\mathbf{r}_1 d^3\mathbf{r}_2=\delta(\mathbf{k}_1+\mathbf{k}_2-\mathbf{k}_1'-\mathbf{k}_2')\langle u_1|u_1'\rangle\langle u_2|u_2'\rangle \times\int d^3\mathbf{r}_{12}\exp\left[\frac{i}{2}\mathbf{r}_{12}\cdot(-\mathbf{k}_1+\mathbf{k}_2)\right]V(\mathbf{r}_{12})\exp\left[\frac{i}{2}\mathbf{r}_{12}\cdot(\mathbf{k}_1'-\mathbf{k}_2')\right] \quad (10)$$

in the bulk. Thus, the Coulomb term in (2) acts only on the envelope and *not* on the lattice periodic Bloch functions. This fact will be used following Eq. (12) and in Eq. (43). Note the conservation of linear momentum in bulk Auger processes.

B. The Auger rate in a more general potential

In a more general potential, such as that of a quantum wire or dot, the translational symmetry of the lattice is lost in certain directions, such as those of quantum confinement. The spatial part of the electron wave function becomes[12]

$$\phi(\mathbf{r})=\sum_{i,\mathbf{k},n} C(\mathbf{k},n)\exp(i\mathbf{k}\cdot\mathbf{R}_i)u_n(\mathbf{k},\mathbf{r}-\mathbf{R}_i)\ , \quad (11)$$

where $\mathbf{R}_i$ denote lattice sites, $\mathbf{k}$ denote wave vectors in the first Brillouin zone, and n is the band index. In general, C must be calculated from an appropriate (tight-binding or $\mathbf{k}\cdot\mathbf{p}$) Hamiltonian, and Eq. (7) becomes very tedious. The first integral in (7) becomes

$$\begin{aligned}\int\int \phi_1^*(\mathbf{r}_1)\phi_2^*(\mathbf{r}_2)V(\mathbf{r}_1-\mathbf{r}_2)\phi_1'(\mathbf{r}_1)\phi_2'(\mathbf{r}_2)d^3\mathbf{r}_1 d^3\mathbf{r}_2 &= \sum_{i1,\mathbf{k}_1,n1}\sum_{i2,\mathbf{k}_2,n2}\sum_{i1',\mathbf{k}_1',n1'}\sum_{i2',\mathbf{k}_2',n2'} C_1^*(\mathbf{k}_1,n1)C_2^*(\mathbf{k}_2,n2)C_1'(\mathbf{k}_1',n1')C_2'(\mathbf{k}_2',n2') \\ &\times\exp[i(-\mathbf{k}_1\cdot\mathbf{R}_{i1}-\mathbf{k}_2\cdot\mathbf{R}_{i2}+\mathbf{k}_1'\cdot\mathbf{R}_{i1}'+\mathbf{k}_2'\cdot\mathbf{R}_{i2}')] \\ &\times\int\int d^3\mathbf{r}_1 d^3\mathbf{r}_2 V(\mathbf{r}_1-\mathbf{r}_2)u_{n1}(\mathbf{k}_1,\mathbf{r}_1-\mathbf{R}_{i1}) \\ &\times u_{n2}(\mathbf{k}_2,\mathbf{r}_2-\mathbf{R}_{i2})u_{n1'}(\mathbf{k}_1',\mathbf{r}_1-\mathbf{R}_{i1}')u_{n2'}(\mathbf{k}_2',\mathbf{r}_2-\mathbf{R}_{i2}')\ . \end{aligned} \quad (12)$$

Equation (9) and the statements following it show that for those Auger processes involving energies in the infrared, $V(\mathbf{R}_{i1}-\mathbf{R}_{i2})$ is slowly varying on the scale of a lattice spacing and can thus be factored out of those integrations over a unit cell. Thus, the exponential term in (12) and all terms to the right of it can be replaced by $V(\mathbf{R}_{i1}-\mathbf{R}_{i2})\times\langle u_{n1}|u_{n1}'\rangle\langle u_{n2}|u_{n2}'\rangle\delta(R_{i1},R_{i1}')\delta(R_{i2},R_{i2}')$. This fact will also be used in (43).

The summations over the lattice sites $i1,i2$ in (12) can be approximated as integrations with the appropriate normalization,

$$\begin{aligned}\int\int \phi_1^*(\mathbf{r}_1)\phi_2^*(\mathbf{r}_2)V(\mathbf{r}_1-\mathbf{r}_2)\phi_1'(\mathbf{r}_1)\phi_2'(\mathbf{r}_2)d^3\mathbf{r}_1 d^3\mathbf{r}_2 &= \sum_{\mathbf{k}_1,n1}\sum_{\mathbf{k}_2,n2}\sum_{\mathbf{k}_1',n1'}\sum_{\mathbf{k}_2',n2'}\langle u_{n1}|u_{n1}'\rangle\langle u_{n2}|u_{n2}'\rangle\frac{1}{V_{\text{unit cell}}^2} \\ &\times\int d^3\mathbf{R}_{i2}\mathcal{F}_{\mathbf{k}_2,n2}^*(\mathbf{R}_{i2})\mathcal{F}_{\mathbf{k}_2',n2'}'(\mathbf{R}_{i2}) \\ &\times\int d^3\mathbf{R}_{i1}\mathcal{F}_{\mathbf{k}_1,n1}^*(\mathbf{R}_{i1})V(\mathbf{R}_{i1}-\mathbf{R}_{i2})\mathcal{F}_{\mathbf{k}_1',n1'}'(\mathbf{R}_{i1}) \end{aligned} \quad (13)$$

where $\mathcal{F}_{\mathbf{k}_j,nj}(\mathbf{R})=C_j(\mathbf{k}_j,nj)\exp\{i\mathbf{k}_j\cdot\mathbf{R}_{ij}\}$, $j=1,2$. Note that the spatial integrals can sometimes be evaluated in closed form; however, the summations over wave vector and band index may be difficult because the Bloch function overlap integrals are functions of these parameters. Observe also that the spatial integrals can be efficiently evaluated numerically even when $\mathcal{F}$ does not have the simple exponential (sinusoidal) spatial dependence. This follows from the fact that the $\mathbf{R}_{i1}$ integral is, mathematically, the electrostatic potential seen at $\mathbf{R}_{i2}$ as a result of the charge distribution $\mathcal{F}_{\mathbf{k}_1,n1}^*(\mathbf{R}_{i1})\mathcal{F}_{\mathbf{k}_1',n1'}'(\mathbf{R}_{i1})$. The vast literature written on solving numerical Dirichlet problems could make the computation of such integrals representing "electrostatic potential" efficient, even when the geometries are complicated (as for a quantum box instead of a quantum sphere), or when the wave functions become complicated (as when the wave functions are solved numerically in the presence of the electron-electron direct and exchange interactions).

For a particular potential with a specific symmetry, Eqs. (6) and (11) can be written in equivalent ways to allow more insight in a (simpler) evaluation of (5). For example, in Sec. IV, we will invoke the spherical symmetry of the quantum dot to write all single and multiparticle states as total-angular-momentum eigenstates.

III. THE USE OF QUANTUM-DOT BARRIER HEIGHTS TO REDUCE THE AUGER RATE

We propose the use of quantum dots in semiconductor lasers to reduce the Auger rate. We note that the Auger rate must be zero when the magnitude of the energy of the final state E_2' is less than the potential barrier formed by the (conduction and valence) band-edge differences between the well and barrier materials. The reason is that when the 2′ state is a bound state of the quantum dot, such a "bound-to- bound" process is really not a true Auger process. Since the Fermi golden rule describing the Auger rate applies only for a time-*dependent* perturbation and since all the bound states of a quantum dot can be solved, at least in principle, using the *complete* Hamiltonian *including* the Coulomb interaction (2), then there is no Auger rate to compute for this time-independent description. Appendix A invokes an example from atomic physics to explain why bound-to-bound processes are not true Auger processes. The Auger rate could be nonzero for bound-to-unbound Auger processes because the 2′ particle is now unbound, and it can leave the vicinity of the quantum dot, thus making the Coulomb interaction time *dependent,* as shown in Fig. 1.

Thus, to greatly reduce the Auger rate, we would like E_2' as required by energy conservation not to lie in a continuum of energy states. One way to do this is to surround the quantum-dot well with very large potential barriers. The potential barrier seen by conduction-band electrons and valence-band holes must be at least $E_{g,w}$, where $E_{g,w}$ is the energy band gap of the well material in the bulk, plus, say, 100 meV. This 100-meV "safety margin" is needed because the quantum-dot energy band gap will be bigger than that in the bulk because of the zero-point energy of the confinement in three dimensions. This 100-meV safety margin is also desirable to eliminate the Auger processes associated with all the occupied states at room temperature. (We choose 100 meV $\simeq 4k_BT$ at room temperature because we expect quantum-dot lasers to be useful for room-temperature operation, where some present day semiconductor lasers cannot operate as a result of these Auger processes.) Thus, in order to greatly reduce the room-temperature Auger rate by using quantum dots, we would like the material serving as the barrier to have a band gap $E_{g,b}$ of at least

$$E_{g,b,\min}=3E_{g,w}+8k_BT=3E_{g,w}+0.2\ \text{eV}\ . \tag{14}$$

This equation is evaluated for various materials in the fourth column of Table I.

It is not enough for the energy band gap of the barrier material to satisfy (14). We also require that the band lineup between the barrier and well materials be such that the discontinuity in both the conduction and valence bands, ΔE_c and ΔE_v, be at least $E_{g,w}$, preferably with an additional 100 meV of added safety margin. These band discontinuities are still the subject of much discussion in both the theoretical and experimental communities.[13–16] No theoretical model appears to explain all semiconductor heterojunction band lineups with complete satisfaction. There is also some error in the measured values of these band lineups. The experimental data seem to agree with the most successful theories to around 0.1 eV, at best, and to about 0.4 eV for junctions involving[13,16–18] HgTe, CdTe, ZnTe, and HgSe.

The last two columns of Table I give the most widely accepted values of the band lineups to date. With the exception of the HgTe-CdTe and InSb-CdTe heterojunctions, for which the measured values[13,18,19] are given, all the band discontinuities are obtained from the transitivity rule and the data given by Margaritondo.[13] The transitivity rule assumes that there is some reference energy level that is constant on both sides of a heterojunction and thus,

$$\Delta E_{c,v}(A,B)=\Delta E_{c,v}(A,C)-\Delta E_{c,v}(B,C) \tag{15}$$

for three semiconductors A, B, C. The band lineups given in Table I are obtained from the most widely accepted value(s) in both theory and experiment, as discussed in a very informative recent review.[13–15]

For realistic quantum-dot lasers, we would also like the well material to be lattice matched to the barrier material.[1] Lattice-matched materials are known to give much better quality laser media in both the bulk and quantum wells because of the removal of surface states, which contribute to loss, associated with point defects in lattice-unmatched materials. Empirically, it appears that[1] a lattice match of about 1.5% or so is absolutely necessary, and a 0.3% accuracy occurs for the best quality semiconductor lasers of today. Thus, we require the lattice constant of the barrier a_b to be related to the lattice constant of the well a_w through

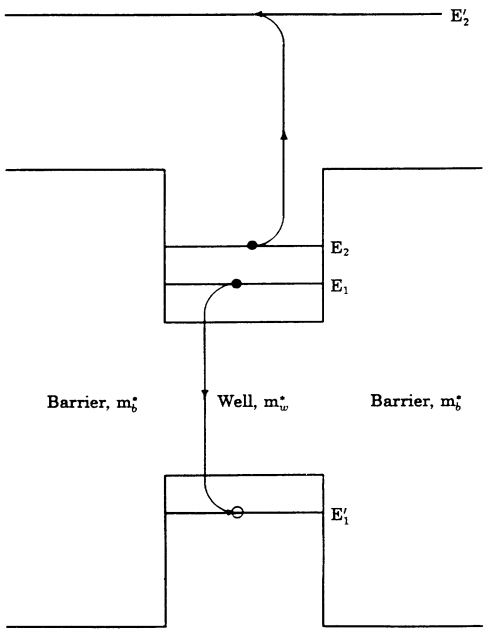

FIG. 1. The energy levels associated with Auger processes in a quantum dot. Bound-to-unbound Auger processes are allowed, as shown here for a *CCCV* process. If energy conservation requires that E_2' be less than the potential barrier, then the Auger rate must be zero (see Sec. III).

TABLE I. The band gaps, lattice constants, and band lineups for possible quantum-dot well and barrier materials. To greatly reduce the Auger rate, the magnitude of the E_2' energy should be less than the potential barrier formed by the (conduction and valence) band-edge differences between the well and barrier materials. Note that no materials were found to satisfy the band gap and lattice constant requirements for In-Ga-As-P, which would be useful in fiber optics. InAs and InSb appear promising as materials for which this Auger rate can be vastly reduced. The band lineups appearing in the last two columns were taken from Margaritondo's review (Ref. 13), except as indicated. The band gap and lattice constant requirements are obtained from (14) and (16). All other data are taken from standard sources (Ref. 20). Compatibility of well and barrier crystal structures is discussed in the text.

Quantum-dot well			Required barrier characteristics		Possible barrier materials				
Material	$E_{g,w}$ (eV)	a_w (Å)	Minimum $E_{g,b}$ (eV)	Possible a_b (Å)	Material	E_g (eV)	a (Å)	ΔE_c (eV)	ΔE_v (eV)
$In_{0.72}Ga_{0.28}As_{0.61}P_{0.39}$	0.9538	5.87	3.06	5.78–5.96					
InAs	0.36	6.0584	1.28	5.968–6.149	ZnTe	2.26	6.101	1.6	0.3
							or	1.2	0.7
					CdSe	1.74	6.05	0.34	1.1
InSb	0.163	6.4788	0.689	6.382–6.576	CdTe	1.44	6.477	0.42	0.85
					CuI	2.95	6.604		2.21[a]
					AgI	2.22	6.502		
					CuCl	3.17	6.42		4.70[a]
HgTe	−0.15	6.4623	0.65	6.365–6.559	CdTe	1.44	6.477		0.1–0.4
HgSe	−0.30	6.084	1.1	5.993–6.175	ZnTe	2.26	6.101		~0.1
					CdSe	1.74	6.05		~0.1
HgS	−0.2	5.8517	0.8	5.764–5.939	InP	1.27	5.86875		
					CdS	2.42	5.832		
Te	0.33	5.91	1.19	5.821–5.999	InP	1.27	5.868 75		
					CdS	2.42	5.832		
PbTe	0.25	6.454	0.95	6.357–6.550	CdTe	1.44	6.477		0.53
SnTe	0.26	6.313	0.98	6.218–6.408					
PbS	0.37	5.9362	1.31	5.847–6.025					
PbSe	0.26	6.1243	0.98	6.032–6.216					
SnSe	0.26	6.02	0.98	5.93–6.110					

[a]Reference 16.

$$0.985 \leq \frac{a_b}{a_w} \leq 1.015 \tag{16}$$

as calculated in the fifth column of Table I. The band gaps and lattice constants given in Table I are obtained from standard sources.[20,21]

Closely related to the issue of lattice matching to avoid defects is the issue of picking well and barrier materials with the same crystal structure. With the exception of the lead salt semiconductors (the last five entries), all of the semiconductors listed in Table I have the zinc-blende structure. We expect that the interface between two lattice-matched, zinc-blende crystals to have a reasonable quality. In fact, we know that HgTe-CdTe,[13] HgSe-CdSe,[22] and InSb-CdTe (Ref. 19) heterojunctions have been successfully grown. The lead salt family of semiconductors have the halite crystal structure. The fabrication of the PbTe-CdTe heterojunction, a halite–zinc-blende junction, has not been reported yet in the literature. However, the PbTe-Ge heterojunction, another halite–zinc-blende junction, has been reported,[13] albeit with some problems at the interface. These problems may make use of halite quantum dots with zinc-blende barriers impractical for lasers. We were not able to find any barrier materials, halite or zinc blende, which fit the band gap and lattice constant constraints discussed above for the last four entries in Table I.

Some comments about Table I are in order. The materials in the first column were chosen to have a band gap in the infrared, where energies are small enough for Auger processes to be strong enough to limit laser action in the bulk. Note that no materials were found to satisfy the band gap and lattice constant requirements for In-Ga-As-P, which would be useful in fiber optics. InAs and InSb appear most promising as materials for which this Auger rate can be vastly reduced. Two values for the band discontinuities for the InAs-ZnTe junction are given, because of discord in the theory and experiment, with the top one being the "more" accepted one. Notice that ΔE_v in the InAs-ZnTe junction and ΔE_c in the InAs-CdSe junction may not be large enough. Perhaps the quaternary Cd-Zn-Te-Se will produce large enough potential barriers in both the conduction and valence bands for InAs quantum dots. Good quality InSb-CdTe heterointerfaces have already been achieved.[19] Theoretical calculations of ΔE_v by Harrison[16] seem to indicate that CuI, but not CuCl, will also make good potential barriers for InSb quantum dots.

The band structures of the inverted band-gap semiconductors HgTe, HgSe, and HgS can be treated with the same formalism as used in this paper. The literature contains much about the HgTe-CdTe and, to a lesser extent, the HgSe-CdSe heterojunctions. Some of the other entries in Table I for these inverted gap semiconductors

provide possibilities that may have better band lineups, although ΔE_c and ΔE_v for these materials are not yet available. The same comments hold true for the semiconductor Te.

Other ways of obtaining a desirable band lineup at a heterointerface

We thus see that it is very likely that InAs and InSb quantum dots surrounded by barriers made of the materials listed in Table I will exhibit very low Auger rates. One wonders if other small band-gap materials that could be lattice matched to a large band-gap material exist. A lot of materials could have the right band lineups, but the lattice-matching requirement rules out most of them. Perhaps one could relax this lattice requirement by growing a monolayer of some other material between the well and the barrier to ease the strain. However, it is likely that there still will be enough strain to cause defects which contribute to laser loss.

Finally, we note that a sheet of dipole charges placed at the heterointerfaces could change the values of ΔE_c and ΔE_v. In fact, the interface dipoles, resulting from quantum-mechanical tunneling, at a heterointerface is one successful model for describing band lineups, as discussed[13,14] in the literature. We now suggest putting artificial delta-doped sheet charges which simulate interface dipoles. Again, the problem with designing the band lineups in this way is that doping the quantum dot could also result in surface states that contribute to laser loss.

IV. THE QUANTUM SPHERE

A zero-dimensional structure with closed-form expressions for both the eigenstates and the Auger rate is a quantum sphere. We calculate the (nonparabolic) band structure and energy states using a multiband envelope-function approximation in eight-band $\mathbf{k}\cdot\mathbf{p}$ theory, which also included some of the effects of higher-order bands. Single-particle and multiparticle eigenstates are chosen to diagonalize the total angular momentum. We present here an analytic expression for the Auger rate in a semiconductor zero-dimensional structure. We will assume infinite potential barriers, which are a good approximation for the very deep potential wells needed to greatly reduce the unwanted bound-to-unbound Auger recombination. We include a practical example in which the room-temperature Auger rate has been reduced by using quantum dots surrounded by large potential energy barriers.

A. Eigenstates in a spherical representation

Recently, it has been shown[23] that in a spherically symmetric potential, such as that near an impurity or that imposed by the energy band-gap differences in the two semiconductors comprising a quantum sphere, the single-electron wave functions must be eigenstates of the total angular momentum $\mathbf{F}$ defined as

$$\mathbf{F}=\mathbf{J}+\mathbf{L}=\mathbf{S}+\mathbf{L}_B+\mathbf{L}\ , \tag{17}$$

where $\mathbf{S}$ is the spin of each electron, of which the z component is $\pm\frac{1}{2}$; $\mathbf{L}_B$ is the "Bloch" angular-momentum operator whose eigenstates denote the $\mathbf{s}$, $\mathbf{p}_x$, $\mathbf{p}_y$, or $\mathbf{p}_z$ nature of the Bloch wave functions near the III-V semiconductor band edge; and $\mathbf{L}$ is the orbital angular-momentum operator associated with the spatial part of the electron's envelope wave function.

As discussed above, in calculating the Auger matrix element, the Coulomb interaction acts only on the envelope part of the wave functions. Thus we have written Eq. (17) so that each of the separate angular-momenta acts on a different coordinate space. That $\mathbf{S}$ should appear separately in the total-angular-momentum operator, (17), is not surprising, since the real space part is decoupled from the spin part of the electron wave function for spin-independent Hamiltonians. The Bloch $\mathbf{L}_B$ and envelope $\mathbf{L}$ angular momenta appear as separate terms in (17) because the Bloch wave functions only have physical significance in the coordinate space inside a unit cell of the lattice, whereas the envelope wave functions are defined on lattice sites only and are considered to be slowly varying over distances comparable to a unit cell. Thus, the Bloch angular momentum and the envelope angular momentum act on state spaces that are effectively separate.

In the standard literature, the $\mathbf{k}\cdot\mathbf{p}$ Hamiltonian is written in the basis of eigenstates $|J,J_z\rangle$ of $\mathbf{J}=\mathbf{S}+\mathbf{L}_B$. This basis is available[23] in the literature. The eigenstates of the envelope angular momentum $\mathbf{L}$ are spherical harmonics: $Y_{L,L_z}(\Omega)=\langle\Omega|L,L_z\rangle$. In a spherically symmetric potential $U(r)$ the radial part of the envelope wave function, which has $Y_{L,L_z}(\Omega)$ as its angular part, satisfies an envelope Schrödinger equation,

$$-\frac{\hbar^2}{2m^*}\frac{d^2[rf(r)]}{dr^2}+\left[U(r)+\frac{L(L+1)\hbar^2}{2m^*r^2}\right](rf(r))=E(rf(r))\ . \tag{18}$$

For $U(r)$ equal to a constant U_0 (as in the well or barrier regions of a quantum sphere) the solutions are spherical Bessel functions of the first kind,

$$f_{nL}(r)=j_L(K_{nL}r)\ , \tag{19}$$

with

$$K_{nL}=\left[\frac{2m^*}{\hbar^2}(E_{nL}-U_0)\right]^{1/2} \tag{20}$$

as the nth value of K_{nL}, which satisfies the boundary conditions. In the well (similarly, for the barrier) region of a quantum sphere, K_{nL} is real (imaginary) for bound states.

1. $\mathbf{k}\cdot\mathbf{p}$ theory with total-angular-momentum eigenstates as a basis

Instead of working with the standard $\mathbf{k}\cdot\mathbf{p}$ Hamiltonian $\langle J,J_z;\mathbf{K}|H|J',J_z';\mathbf{K}\rangle$ and its basis $|J_i',J_{iz}'\rangle$, we work with a unitary transformation of the Hamiltonian UHU^{-1}, which diagonalizes total angular momentum and its corresponding basis $U|J_i',J_{iz}'\rangle$. The unitary transformation that allows the $\mathbf{k}\cdot\mathbf{p}$ Hamiltonian in the $|F_i',F_{iz}';J_i'L_i';K\rangle$ basis to be written in terms of the standard $\mathbf{k}\cdot\mathbf{p}$ Hamiltonian, $\langle J,J_z;\mathbf{K}|H|J',J_z';\mathbf{K}\rangle$ was recently derived,[23]

$$\langle F,F_z;J,L;K|H|F',F'_z;J',L';K\rangle=\sum_{J_z=-J}^{J}\sum_{J'_z=-J'}^{J'}\langle J,J_z;L,L_z=F_z-J_z|F,F_z;J,L\rangle \times\langle J',J'_z;L',L_z=F'_z-J'_z|F',F'_z;J',L'\rangle \times\int d\Omega_{\mathbf{k}}Y^{*}_{L,(F_z-J_z)}(\Omega_{\mathbf{K}})Y_{L',(F'_z-J'_z)}(\Omega_{\mathbf{K}})\langle J,J_z;\mathbf{K}|H|J',J'_z;\mathbf{K}\rangle \ . \quad (21)$$

The standard $\mathbf{k}\cdot\mathbf{p}$ Hamiltonian is given[23] in the literature. The parameters we used in this Hamiltonian are given in Appendix B. Note that since the $\mathbf{k}\cdot\mathbf{p}$ Hamiltonian in the standard $|J'_i,J'_{iz}\rangle$ basis was constructed to include remote bands, the overlap integrals[24] of the Bloch functions should be reasonably accurate.

The energy eigenstates in a quantum sphere must also be eigenstates of the total angular momentum $\mathbf{F}$. To obtain these eigenstates, we use the same unitary transformation that helped us to transform the Hamiltonian (21). Thus, we can write the energy eigenstates $\Phi'_{i'}(\tau)$ as ,

$$\begin{aligned}\Phi'_{i'}(\tau)&=\langle\tau|F'_i,F'_{iz}\rangle\\&=\sum_{J'_i,L'_i}C_{K,J'_i,L'_i}f_{L'_i}(Kr)\sum_{J'_{iz}=-J'_i}^{J'_i}\sum_{L'_{iz}=-L'_i}^{L'_i}\langle\sigma_{J'_i}|J'_i,J'_{iz}\rangle Y_{L'_i,L'_{iz}}(\Omega)\langle J'_i,J'_{iz};L'_i,L'_{iz};K|J'_i,L'_i;F'_i,F'_{iz};K\rangle\\&=\sum_{J'_i,L'_i}C_{K,J'_i,L'_i}f_{L'_i}(Kr)\langle\sigma_{J'_i},\Omega|J'_i,L'_i;F'_i,F'_{iz}\rangle \ , \end{aligned} \quad (22)$$

where $f_{L'_i}(Kr)$ is the radial part of the envelope function for each different angular-momentum term in (28) and (30), where K is determined by the external potential $U(r)$, where $\sigma_{J'_i}$ is now the spin coordinate associated with J'_i, Ω is the angular part of the spatial coordinates, where $\langle J'_i,J'_{iz};L'_i,L'_{iz};K|J'_i,L'_i;F'_i,F'_{iz};K\rangle$ is a Clebsch-Gordan coefficient, and where

$$C_{K,J'_i,L'_i}=\langle J'_i,L'_i;F'_i,F'_{iz};K|F'_i,F'_{iz};K\rangle \quad (23)$$

are determined by diagonalizing the $\mathbf{k}\cdot\mathbf{p}$ Hamiltonian in the $|F'_i,F'_{iz};J'_i,L'_i\rangle$ basis.

The $\mathbf{k}\cdot\mathbf{p}$ Hamiltonian in the $|F'_i,F'_{iz};J'_i,L'_i\rangle$ basis has been diagonalized for $F=\frac{1}{2},\frac{3}{2}$ by Sercel and Vahala.[23] In general, one can show that for $F\geq\frac{3}{2}$, this 8×8 $\mathbf{k}\cdot\mathbf{p}$ Hamiltonian in the $|F'_i,F'_{iz};J'_i,L'_i\rangle$ basis is block diagonal because of parity selection rules. Each of the two blocks ($p=0,1$) has the form

$$H_{F,p=0,1}=\begin{bmatrix} E_c+\frac{1}{2}K^2 & igPK & ihPK & ijPK \\ -igPK & E_v-\frac{\gamma_1K^2}{2}+a\frac{\gamma_2K^2}{2} & b\frac{\gamma_2K^2}{2} & c\frac{\gamma_2K^2}{2} \\ -ihPK & b\frac{\gamma_2K^2}{2} & E_v-\frac{\gamma_1K^2}{2}-a\frac{\gamma_2K^2}{2} & d\frac{\gamma_2K^2}{2} \\ -ijPK & c\frac{\gamma_2K^2}{2} & d\frac{\gamma_2K^2}{2} & E_-\frac{\gamma_1k^2}{2}-\Delta \end{bmatrix} \quad (24)$$

for total angular momentum F greater than or equal to $\frac{3}{2}$. The $F=\frac{1}{2}$ Hamiltonian was given previously.[23] Here, $E_{c,v}$ are the conduction- and valence-band-edge energies P is the Kane momentum matrix element, $i=\sqrt{-1},\gamma_i$ are the modified Luttinger parameters[23] as discussed in Appendix B, and $K^2=K_x^2+K_y^2+K_z^2$. Numerical values for the constants a,b,c,d,g,h,j in (24) are listed in Table II. The bases $|F'_i,F'_{iz};J'_i,L'_i\rangle$ for each of the two Hamiltonians (24) are listed in (25) and (26) below.

One of the 4×4 Hamiltonians (24) has the energy eigenstates (simultaneously eigenstates of the total angular momentum with the eigenvalues F,F_z) ($p=1$),

$$\begin{aligned}\Phi(\tau)=&A\langle\sigma\Omega r|J=\tfrac{1}{2},L=F+\tfrac{1}{2};K\rangle_C\\&+B\langle\sigma\Omega r|J=\tfrac{3}{2},L=F-\tfrac{1}{2};K\rangle\\&+C\langle\sigma\Omega r|J=\tfrac{3}{2},L=F+\tfrac{3}{2};K\rangle\\&+D\langle\sigma\Omega r|J=\tfrac{1}{2},L=F-\tfrac{1}{2};K\rangle_S \ , \end{aligned} \quad (25)$$

and the other has eigenstates ($p=0$),

$$\Phi(\tau)=A\langle\sigma\Omega r|J=\tfrac{1}{2},L=F-\tfrac{1}{2};K\rangle_C +B\langle\sigma\Omega r|J=\tfrac{3}{2},L=F-\tfrac{3}{2};K\rangle +C\langle\sigma\Omega r|J=\tfrac{3}{2},L=F+\tfrac{1}{2};K\rangle +D\langle\sigma\Omega r|J=\tfrac{1}{2},L=F+\tfrac{1}{2};K\rangle_S \ . \quad (26)$$

The subscripts C and S distinguish between the conduction and split-off hole bands for the $J=\frac{1}{2}$ case. The constants A,B,C,D, are the coefficients (23) determined by explicitly finding the four eigenvectors of each of the 4×4 Hamiltonians. Remember that each of the two 4×4 Hamiltonians has four eigenvectors whose eigenvalues are the electron, heavy-hole, light-hole, and split-off hole energies at a particular wave vector.

2. *Finding the bound-state energies and wave functions: band mixing*

In our studies, we want our quantum dots to be surrounded by large potential energy barriers, so that the bound-to-unbound Auger rate is minimized. Thus we can approximate the bound-state energies by finding those energies that force the radial part of the envelope wave function in (22) to vanish. We illustrate this point by generalizing an example found[23] in the literature.

As discussed in the literature,[23] for hole energies that are close enough to the valence-band edge such that the conduction and split-off hole bands seem remote, the Hamiltonian (24) can be approximated by the 2×2 matrix sitting at its center, with the modified Luttinger parameters replaced by the true Luttinger parameters. These bound hole states have energies E with wave vectors satisfying

$$(a+2)^2 j_{L2}(K_{HH}R)j_{L3}(K_{LH}R) +b^2 j_{L2}(K_{LH}R)j_{L3}(K_{HH}R)=0 \ . \quad (27)$$

For these bound hole states, the corresponding wave functions are

$$\Phi_H(\tau)=\{\langle\sigma\Omega|J=\tfrac{3}{2},L=L2\rangle(-b)j_{L3}(K_{HH}R)[j_{L2}(K_{LH}R)j_{L2}(K_{HH}r)-j_{L2}(K_{HH}R)j_{L2}(K_{LH}r)] +\langle\sigma\Omega|J=\tfrac{3}{2},L=L3\rangle(a+2)j_{L2}(K_{HH}R)[j_{L3}(K_{LH}R)j_{L3}(K_{HH}r)-j_{L3}(K_{\rm HH}R)j_{L3}(K_{LH}r)]\} \quad (28)$$

TABLE II. Numerical values for the a,b,c,d,g,h,j constants in the Hamiltonian (24). This Hamiltonian, expressed in a basis of total-angular-momentum eigenstates $|F_i',F_{iz}';J_i',L_i';K\rangle$, is obtained from a unitary transformation of the standard $\mathbf{k}\cdot\mathbf{p}$ Hamiltonian given in the (Ref. 23) literature. F is the total-angular-momentum quantum number. Note that the numbers for $F=\frac{3}{2}$ match those given in the literature (Ref. 23).

F	p	g	h	j	a	b	c	d
1.5	0	0.577 350 27	−0.577 350 27	−0.577 350 27	0.000 000 00	2.000 000 00	2.000 000 00	−2.000 000 00
1.5	1	0.258 198 89	−0.774 596 67	−0.577 350 27	1.600 000 00	1.200 000 00	0.894 427 19	−2.683 281 57
2.5	0	0.632 455 53	−0.516 397 78	−0.577 350 27	−0.400 000 00	1.959 591 79	2.190 890 23	−1.788 854 38
2.5	1	0.308 606 70	−0.755 928 95	−0.577 350 27	1.428 571 43	1.399 708 42	1.069 044 97	−2.618 614 68
3.5	0	0.654 653 67	−0.487 950 04	−0.577 350 27	−0.571 428 57	1.916 629 70	2.267 786 84	−1.690 308 51
3.5	1	0.333 333 33	−0.745 355 99	−0.577 350 27	1.333 333 33	1.490 711 99	1.154 700 54	−2.581 988 90
4.5	0	0.666 666 67	−0.471 404 52	−0.577 350 27	−0.666 666 67	1.885 618 08	2.309 401 08	−1.632 993 16
4.5	1	0.348 155 31	−0.738 548 95	−0.577 350 27	1.272 727 27	1.542 778 43	1.206 045 38	−2.558 408 60
5.5	0	0.674 199 86	−0.460 566 19	−0.577 350 27	−0.727 272 73	1.863 081 96	2.335 496 83	−1.595 448 07
5.5	1	0.358 057 44	−0.733 799 39	−0.577 350 27	1.230 769 23	1.576 453 96	1.240 347 35	−2.541 955 64
6.5	0	0.679 366 22	−0.452 910 81	−0.577 350 27	−0.769 230 77	1.846 153 85	2.353 393 62	−1.568 929 08
6.5	1	0.365 148 37	−0.730 296 74	−0.577 350 27	1.200 000 00	1.600 000 00	1.264 911 06	−2.529 822 13
7.5	0	0.683 130 05	−0.447 213 60	−0.577 350 27	−0.800 000 00	1.833 030 28	2.366 431 91	−1.549 193 34
7.5	1	0.370 479 29	−0.727 606 88	−0.577 350 27	1.176 470 59	1.617 379 66	1.283 377 90	−2.520 504 15
8.5	0	0.685 994 34	−0.442 807 44	−0.577 350 27	−0.823 529 41	1.822 580 40	2.376 354 10	−1.533 929 98
8.5	1	0.374 634 32	−0.725 476 25	−0.577 350 27	1.157 894 74	1.630 729 83	1.297 771 37	−2.513 123 45
9.5	0	0.688 247 20	−0.439 297 69	−0.577 350 27	−0.842 105 26	1.814 072 42	2.384 158 24	−1.521 771 82
9.5	1	0.377 964 47	−0.723 746 86	−0.577 350 27	1.142 857 14	1.641 303 61	1.309 307 34	−2.507 132 68
10.5	0	0.690 065 56	−0.436 435 78	−0.577 350 27	−0.857 142 86	1.807 015 81	2.390 457 22	−1.511 857 89
10.5	1	0.380 693 49	−0.722 315 12	−0.577 350 27	1.130 434 78	1.649 884 00	1.318 760 95	−2.502 172 97
11.5	0	0.691 564 07	−0.434 057 37	−0.577 350 27	−0.869 565 22	1.801 070 89	2.395 648 23	−1.503 618 82
11.5	1	0.382 970 84	−0.721 110 26	−0.577 350 27	1.120 000 00	1.656 985 21	1.326 649 92	−2.497 999 20
12.5	0	0.692 820 32	−0.432 049 38	−0.577 350 27	−0.880 000 00	1.795 995 55	2.400 000 00	−1.496 662 95
12.5	1	0.384 900 18	−0.720 082 30	−0.577 350 27	1.111 111 11	1.662 958 84	1.333 333 33	−2.494 438 26

to within an overall multiplicative normalization factor.

Equation (27) is useful when the conduction-band states are treated as decoupled from the valence bands. In our numerical models, however, we diagonalized the full (for $F \geq \frac{3}{2}$) 8×8 Hamiltonian (21), whose two 4×4 blocks each has four eigenstates of the form (25) or (26). The $F=\frac{1}{2}$ Hamiltonian and eigenstates appear[23] explicitly in the literature. Thus, in our numerical model, the conduction- (valence-) band states necessarily have some valence- (conduction-) band character, according to (25) and (26). Our energies are found by requiring that the envelope wave functions of the dominant terms [the first term of (25) and (26) for conduction-band states and the next two terms of (25) and (26) for valence states] in (25) vanish on the surface of the quantum dot. In our model, the bulk energy bands $E(K_{C,\mathrm{LH,HH,SOH}})$ are nonparabolic functions of the wave vector, according to (24).

To include conduction-band (and split-off hole) character in the hole wave functions, note that complex wave vectors,[25,26] and thus modified spherical Bessel functions, must appear in the equation above because real wave vectors are associated with energies *above* the conduction-band edge (or *below* the split-off hole band edge). These complex wave vectors and modified spherical Bessel functions correspond to Tamm states, which often appear in surface science studies,[25,26] where the translational symmetry of the bulk semiconductor is lost.

For the bound electron states, we could simply ignore the Tamm states and choose the two conduction-band eigenvector(s) of the eight represented by (25) and (26) such that the conduction-band part of these wave functions [the first terms in (25) and (26)] vanish at $r=R$ for all angles. This is equivalent to to what is usually done in quantum-well calculations. Such a description would be appropriate for electron energies that are close to the bulk band edge. For energies further from the conduction-band edge, we should include some valence-band character in the form of Tamm states in the conduction-band wave functions. This is illustrated below.

As conduction-band energies become further removed from the conduction-band edge, $\mathbf{k}\cdot\mathbf{p}$ theory tells us that the conduction-band wave functions will pick up some valence-band character which is mostly light hole. The reason is that the split-off hole band is further away from the conduction band than the light-hole band; and the heavy-hole band couples to the conduction band through remote bands only. All of this should be clear from the standard $\mathbf{k}\cdot\mathbf{p}$ Hamiltonian. One can show that the most strongly bound electron states have energies E with wave vectors satisfying

$$j_0(K_C R)j_1(i\mathcal{K}R)+\frac{\frac{2}{3}P^2K_C i\mathcal{K}}{(E_C-E_V)^2}j_0(i\mathcal{K}R)j_1(K_C R)=0 \tag{29}$$

analogous to (27) above. Note that the hole wave vectors $i\mathcal{K}$ are imaginary in Eq. (29) when we are solving for conduction-band states, for which $E=E_C(K_C)\equiv E_{\mathrm{LH}}(i\mathcal{K})$. The ground-state electron energy has the form, to within a normalization factor,

$$\Phi_c(\tau)=\left\{\langle\sigma\Omega|J=\tfrac{1}{2},L=0\rangle j_1(i\mathcal{K}R)[j_0(i\mathcal{K}R)j_0(K_C r)-j_0(K_C R)j_0(i\mathcal{K}r)]\right.$$
$$\left.+\langle\sigma\Omega|J=\tfrac{3}{2},L=1\rangle i\left[\frac{E-E_C}{E-E_V}\right]^{1/2}j_0(i\mathcal{K}R)[j_1(i\mathcal{K}R)j_1(K_C r)-j_1(K_C R)j_1(i\mathcal{K}r)]\right\}, \tag{30}$$

where the evanescent Tamm[25,26] states $j_n(i\mathcal{K}r)$ should be included. Numerically, we found that the Tamm states contribute about 15% to both the single-particle conduction-band energies and the Auger Slater integrals. After noting the size of their contribution, these Tamm states were not included in our first cut, rough calculation because we felt that an error of this magnitude is easily available from uncertainties in our band parameters, especially the band lineups.[14]

When the Tamm states are not included, Eq. (30) reduces to

$$\Phi_c(\tau)=A'_C\left\{j_0(K_C r)\langle\sigma\Omega|J=\tfrac{1}{2},L=0\rangle+i\left[\frac{E-E_C}{E-E_V}\right]^{1/2}j_1(K_C r)\langle\sigma\Omega|J=\tfrac{3}{2},L=1\rangle\right\}, \tag{31}$$

as in the literature.[23]

Because of the recent interest in quantum-box lasers, we may be interested in calculating the induced dipole between any conduction-band electron and any valence-band hole. Observe that in calculating the gain proportional to the square of the dipole between these two states of a quantum-box laser, one must note that the overlap integral between the envelope functions of the two aforementioned ground states is not unity, as had previously been assumed,[8] because the hole ground state is an admixture[23,27] of light- and heavy-hole states.

3. *Multiparticle states*

In calculating the Auger rate, we used Eq. (5), and thus assumed that the initial and final states have the form (3). Antisymmetry with respect to two particle interchanges as in (3) is not the only requirement for our wave functions. We also require that in this spherically symmetric system, multiparticle states must diagonalize the total multiparticle angular momentum, which is a sum of terms like (17). In atomic physics, these two requirements, eigenstates of total angular momentum and of the

correct antisymmetry, are met through the use of[11,28] recoupling coefficients and[11,29] coefficients of fractional parentage.

Recoupling coefficients are needed whenever three or more angular momenta are added together. The reason is that there are a number of different ways to choose which two angular momenta are added together first and in what order the remaining angular momenta are to be coupled to the first two. The product of the square-rooted quantities and the three Racah coefficients in the last three lines of (54) below is analogous to the recoupling coefficients of atomic physics. The coefficients of fractional parentage are found by requiring that the correct linear combination of recoupled angular momenta states be antisymmetric with respect to two-particle interchanges. When there are no more than two particles in each single-particle energy level, as in the case computed below with just two electrons and two holes, the formalism of the coefficients of fractional parentage is not needed.

It is well known in semiconductor physics that the conduction-band electrons and valence-band holes will thermalize independently of each other and will have separate Fermi energies. Thus, at this order of approximation, we can recouple angular momenta in the following way. We will assume that the two initial electrons involved in a *CCCV* Auger process (the two initial holes involved in a *CVVV* Auger process) have a definite angular momentum, as do all single-particle states and the total N_{elec} system. Since the Coulomb interaction potential is rotationally invariant, the two final electrons resulting from a *CCCV* Auger process (the two final holes resulting from a *CVVV* Auger process) must also have a definite angular momentum. Thus, we write the initial and final states as those linear combinations of Slater determinants (3), which allow us to replace $|\Phi_1\rangle|\Phi_2\rangle$ by

$$|F_1,F_2;F,F_z\rangle=\sum_{F_{1z},(F_{2z}=F_z-F_{1z})}|F_1,F_{1z}\rangle|F_2,F_{2z}\rangle \times\langle F_1,F_{1z};F_2,F_{2z}|F_1,F_2;F,F_z\rangle\ , \quad (32)$$

and $|\Phi_1'\rangle|\Phi_2'\rangle$ by

$$|F_1',F_2';F',F_z'\rangle=\sum_{F_{1z}'(F_{2z}'=F_z'-F_{1z}')}|F_1',F_{1z}'\rangle|F_2',F_{2z}'\rangle \times\langle|F_1',F_{1z}';F_2',F_{2z}'|F_1',F_2';F',F_z'\rangle \quad (33)$$

in (5).

In our calculations, we will use single-particle states in (3) and single-particle energy levels. The reason is that we expect the electrons to be weakly interacting; our numerical calculations indicate that the Coulomb repulsion energy between particles is just a few meV, which is smaller than the bound-state zero-point energies which are of the order of 10–100 meV. Including the Coulomb interaction between particles in a more precise fashion is not sensible since the band parameters are often not precisely known. In particular, the band lineups have an error of[13–15] at least 100 meV for the small band-gap materials in which the bulk Auger rates are large. Such errors would allow more unbound states to be accessible as final states in an Auger process. Equation (3) should be a good approximation (for weakly interacting particles) to the actual multiparticle states because the form of this equation is what one would expect when the Coulomb and exchange interaction between particles are accounted for. The general conclusions of this work with respect to trends in and elimination of the Auger rate are not expected to be modified much by inclusion of the electron-electron Coulomb interaction.

4. *Notation for single-particle states*

We will label single-particle states as $n(L)_F$ (e.g., $1S_{3/2}$) where n denotes which orbital, e.g., which root of (27) to take; F is the single-particle total-angular-momentum quantum number; and where (L) is a letter $(S,P,D,\ldots)$ denoting the envelope angular momentum of the dominant portion of the wave function. This dominant portion of the wave function is the first term of (25) or (26) for conduction-band states. For hole states, this "dominant" portion is a misnomer because the heavy- and light-hole states both mix the second and third terms in (25) and (26). For $F\geq\frac{3}{2}$ holes, we use the second term in (25) and (26) because in the absence of $\mathbf{k}\cdot\mathbf{p}$ theory, the second and third terms in (25) and (26) would not be mixed. For $F=\frac{1}{2}$ holes, we use the third term in these equations because the second term does not exist.[23] The implicit assumption in this notation is that the microscopic (Bloch periodic) part of the wave functions in all conduction-band states have $J=\frac{1}{2}$, and all light- and heavy-hole valence-band states have $J=\frac{3}{2}$.

B. The Auger rate in a quantum sphere

In calculating the Auger rate in a quantum sphere, we will denote the initial particles as 1,2, and the final particles as 1′, 2′. In our notation, particles 1, 2, and 2′ will always be in the same band. Thus, for *CCCV* (similarly, for *CVVV*) processes, particles 1, 2, and 2′ are electrons (holes for *CVVV*) and particle 1′ is a hole (electron). In our quantum-sphere calculation, we will assume that there are only two electrons and two holes in the sphere so that we can use (32) and (33) without finding the coefficients of fractional parentage.

1. *The bound-to-unbound Auger rate in a quantum dot*

If all four energy states E_1,E_2,E_1',E_2' involved in an Auger process are bound (discrete) states, then the Auger rate for that process in a quantum dot is zero, as we discuss in Sec. III. Thus, all we need is to find expressions for the bound-to-unbound Auger rates in a quantum dot. From (1), this rate is

$$R_A=\frac{2\pi}{\hbar}\frac{1}{N_{\text{initial}}}\sum_{\text{initial states}}\sum_{\text{final states}}|V_{if}|^2\delta(E_i-E_f)P(1,2,1',2')g(E_2') , \tag{34}$$

where the joint probability of occupation is, for a *CCCV* process,

$$P(1,1',2,2')=f_c(E_1)f_c(E_2)f_v(E_{1'})[1-f_c(E_{2'})]-[1-f_c(E_1)][1-f_c(E_2)][1-f_v(E_{1'})]f_c(E_{2'}) \tag{35}$$

with $f_c(E)$ and $f_v(E)$ as Fermi-Dirac occupation probabilities at temperature T,

$$f_{c,v}(E)=\frac{1}{1+\exp\left[\dfrac{E-E_{fc,fv}}{K_BT}\right]} . \tag{36}$$

These formulas come from a grand canonical ensemble for weakly interacting, identical particles.

2. *The density of final states*

The density of final states $g(E_2')$ for a bound-to-unbound Auger process in a quantum dot is the bulk density of states (per unit volume) in the *barrier* material,

$$g(E)=\begin{cases}\dfrac{1}{4\pi^2}\left[\dfrac{2m_0}{\hbar^2}\right]^{3/2}(E_2'-V_B)^{1/2}\left[\dfrac{m^*_{\text{barr},c}}{m_0}\right]^{3/2} & \text{for electrons}\\ \dfrac{1}{4\pi^2}\left[\dfrac{2m_0}{\hbar^2}\right]^{3/2}(E_2'-V_B)^{1/2}\left[\left[\dfrac{m^*_{\text{barr,lh}}}{m_0}\right]^{3/2}+\left[\dfrac{m^*_{\text{barr,hh}}}{m_0}\right]^{3/2}\right] & \text{for holes ,}\end{cases} \tag{37}$$

where V_B is the barrier height, the effective masses are those in the barrier region, m_0 is the free electron mass, and where we have assumed that the energy bands in the barrier material have a parabolic dispersion relation. This is a valid assumption when E_2' is close to the barrier band edge: $E_2'-V_B$ small. Note that there is no extra factor of 2 for spin degeneracy in (37) because the different spins of the continuum states will be summed over explicitly.

In counting the number of states, boundary conditions (either set the wave function equal to zero at some large distance from the quantum dot or use periodic boundary conditions) are applied to the wave functions in the *barrier* region, which is the region that looks infinitely large. Equation (37) is exact for continuum states in the conduction band because there is a one-to-one correspondence between the wave vectors calculated for states in the barrier region and those in the well region. Equation (37) is *not* exact for continuum states in the valence band, because as we have seen above, the spherically symmetric quantum-dot barriers necessarily mix the heavy-hole, light-hole, and split-off hole states. Each type of hole has a different energy wave-vector dispersion relation. The correct hole density of states is obtained by finding the precise hole wave functions in the barrier and well regions. At the heterointerface, we demand continuity of the wave function and its derivative. (In practice, this is often done only for the envelope part and not the lattice periodic part of the wave function, a procedure which is not correct by first principles.) The density of states is found by counting the number of states per unit energy which satisfies the boundary conditions at the edge of the semiconductor wafer sample. To perform the calculation precisely is very hard because the boundary condition at infinity (the edge of the semiconductor wafer sample) is an equation in terms of sums of products of six or more modified and ordinary spherical Bessel functions. [For holes, this equation for the boundary condition at infinity is determined mainly by the largest wave vector associated with the wave function, which is the heavy-hole wave vector. Equation (37) is thus a good approximation, especially if the heavy-hole mass is a lot bigger than the light-hole mass in the barrier region, for the hole density of states because each continuum hole state must have some heavy-hole character in the barrier region.] Of course, in the limit that the quantum-dot radius becomes very large and E_2' becomes large compared to the barrier height, Eq. (37) becomes exact.

3. *Calculating the matrix element*

In preparation for calculating the Auger rate matrix element, we expand the screened Coulomb potential in terms of radial and angular parts,

$$\frac{\exp(-\lambda|\mathbf{r}_1-\mathbf{r}_2|)}{\lambda|\mathbf{r}_1-\mathbf{r}_2|}=\sum_{l=0}^{\infty}\sum_{m=-l}^{l}4\pi\frac{I_{l+1/2}(\lambda r_<)}{\sqrt{\lambda r_<}}\frac{K_{l+1/2}(\lambda r_>)}{\sqrt{\lambda r_>}}Y^*_{lm}(\theta_1,\phi_1)Y_{lm}(\theta_2,\phi_2) , \tag{38}$$

where $\theta_i,\phi_i,\Omega_i,i=1,2$, are angles in spherical coordinates; and $I_{l+1/2}(\lambda r_<)$, $K_{l+1/2}(\lambda r_>)$ are[30] modified spherical Bessel functions of the first and third kinds, respectively. The inverse screening length λ is very small for dynamic[31]

processes such as Auger recombination and is usually taken to be zero. Thus, the expression above reduces to the familiar expansion of the Coulomb potential in terms of 2^l pole moments,

$$\frac{1}{|\mathbf{r}_1-\mathbf{r}_2|}=\sum_{l=0}^{\infty}\left[\frac{4\pi}{2l+1}\right]\frac{r_<^l}{r_>^{l+1}}\sum_{m=-l}^{l}Y_{lm}^*(\theta_1,\phi_1)Y_{lm}(\theta_2,\phi_2)\ , \tag{39}$$

where

$$Y_{lm}^*(\Omega_1)=(-1)^m Y_{l,-m}(\Omega_1)\ . \tag{40}$$

Using the notation of (4), we evaluate the direct term in the integral (5) above,

$$\begin{aligned}D&\equiv\int\int d\tau_1 d\tau_2\phi_1^*(\tau_1)\phi_2^*(\tau_2)V(\mathbf{r}_1-\mathbf{r}_2)\phi_1'(\tau_1)\phi_2'(\tau_2)\\&=\int d\tau_2\phi_2^*(\tau_2)\phi_2'(\tau_2)\int d\tau_1\phi_1^*(\tau_1)\phi_1'(\tau_1)\frac{1}{|\mathbf{r}_1-\mathbf{r}_2|}\ .\end{aligned} \tag{41}$$

Using the reasoning of Eqs. (9) and (10), the integral of interest can be written with the help of (32) and (33) as,

$$\begin{aligned}D&=\left\langle F_1,F_2;F,F_z\left|\frac{1}{|\mathbf{r}_1-\mathbf{r}_2|}\right|F_1',F_2';F',F_z'\right\rangle\\&=\sum_{F_{1z},(F_{2z}=F_z-F_{1z})}\sum_{F_{1z}',(F_{2z}'=F_z'-F_{1z}')}\langle F_1,F_{1z};F_2,F_{2z}|F_1,F_2;F,F_z\rangle\langle F_1',F_{1z}';F_2',F_{2z}'|F_1',F_2';F',F_z'\rangle\\&\qquad\times\left\langle F_1,F_{1z};F_2,F_{2z}\left|\frac{1}{|\mathbf{r}_1-\mathbf{r}_2|}\right|F_1',F_{1z}';F_2',F_{2z}'\right\rangle\ .\end{aligned} \tag{42}$$

Use of (22) gives

$$\begin{aligned}&\left\langle F_1,F_{1z};F_2,F_{2z}\left|\frac{1}{|\mathbf{r}_1-\mathbf{r}_2|}\right|F_1',F_{1z}';F_2',F_{2z}'\right\rangle\\&=\sum_{J_2,L_2,J_2',L_2'}C^*_{K_2,J_2,L_2}C_{K_2',J_2',L_2'}\\&\qquad\times\sum_{J_1,L_1,J_1',L_1'}C^*_{K_1,J_1,L_1}C_{K_1',J_1',L_1'}\sum_{l=0}^{\infty}R_l(1,2,1',2')\\&\qquad\qquad\times\sum_{m=-l}^{l}(-1)^m\langle J_1,L_1;F_1,F_{1z}|Y_{l,-m}|J_1',L_1';F_1',F_{1z}'\rangle\\&\qquad\qquad\times\langle J_2,L_2;F_2,F_{2z}|Y_{l,m}|J_2',L_2';F_2',F_{2z}'\rangle\ ,\end{aligned} \tag{43}$$

where the Slater integrals are

$$R_l(1,2,1',2')=\int_0^{\infty}r_2^2dr_2\int_0^{\infty}r_1^2dr_1 f_{L_2}^*(K_2r_2)f_{L_2'}(K_2'r_2)\frac{4\pi}{2l+1}\frac{r_<^l}{r_>^{l+1}}f_{L_1}^*(K_1r_1)f_{L_1'}(K_1'r_1)\ , \tag{44}$$

and where R is the radius of the quantum dot; where $f_{L_i}(Kr)$ is the radial part of the envelope function for each different angular momentum term in (28), (30), (25), and (26); and where the standard basis of Bloch functions $|J_i,J_{iz}\rangle$, at the Γ point have the normalization,

$$\langle J_i,J_{iz}|J_i',J_{iz}'\rangle=\delta_{J_i,J_i'}\delta_{J_{iz},J_{iz}'}\ . \tag{45}$$

Appendix C discusses a numerical method for evaluating Slater integrals by solving a second-order ordinary differential equation. From the discussion in Appendix C, the r_1 integral in (44), defined as $\tilde{V}_l(r_2;L_1,L_1',K_1,K_1')\equiv\tilde{V}_l(r_2)$, satisfies

$$\left[\frac{d^2}{dr^2}-\frac{l(l+1)}{r^2}\right][r\tilde{V}_l(r)]=-4\pi[rf_{L_1}^*(K_1r)f_{L_1'}(K_1'r)]\ , \tag{46}$$

an equation whose numerical solution we can find.

Remembering that σ now denotes the spin coordinates of **J**, which is not acted on by Y_{lm}, we can use Racah coefficients $W(abcd;ef)$ to write the angular integrals, using standard phase conventions[10,32] in (43) as

$$\langle J_1,L_1;F_1,F_{1z}|Y_{l,-m}|J_1',L_1';F_1',F_{1z}'\rangle=\delta_{F_{1z},-m+F_{1z}'}\delta_{J_1,J_1'}\langle L_1\|l\|L_1'\rangle\langle l,-m;F_1',F_{1z}'|l,F_1';F_1,F_{1z}\rangle$$
$$\times[(2F_1'+1)(2L_1+1)]^{1/2}W(lL_1'F_1J_1;L_1F_1')(-1)^{3l-2L_1'+6J_1+F_1+F_1'}, \quad (47)$$

$$\langle J_2,L_2;F_2,F_{2z}|Y_{l,m}|J_2',L_2';F_2',F_{2z}'\rangle=\delta_{F_{2z},m+F_{2z}'}\delta_{J_2,J_2'}\langle L_2\|l\|L_2'\rangle\langle l,m;F_2',F_{2z}'|l,F_2';F_2,F_{2z}\rangle$$
$$\times[(2F_2'+1)(2L_2+1)]^{1/2}W(lL_2'F_2J_2;L_2F_2')(-1)^{3l-2L_2'+6J_2+F_2+F_2'}, \quad (48)$$

where we have invoked the Wigner-Eckart theorem,

$$\langle L_2,L_{2z}|Y_{lm}|L_2',L_{2z}'\rangle=\delta_{L_{2z},m+L_{2z}'}\langle L_2',L_{2z}';l,m|L_2',l;L_2,L_{2z}\rangle\langle L_2\|l\|L_2'\rangle\ , \quad (49)$$

$$\langle L_1,L_{1z}|Y_{l,-m}|L_1',L_{1z}'\rangle=\delta_{L_{1z},-m+L_{1z}'}\langle L_1',L_{1z}';l,-m|L_1',l;L_1,L_{1z}\rangle\langle L_1\|l\|L_1'\rangle\ , \quad (50)$$

and where the reduced matrix elements are

$$\langle L\|l\|L'\rangle=(-1)^{l-L'}\left[\frac{(2l+1)(2L'+1)}{4\pi}\right]^{1/2}\begin{bmatrix}l & L' & L\\ 0 & 0 & 0\end{bmatrix}. \quad (51)$$

The $3j$ symbol above is nonzero when $l+L'+L\equiv J_s$ is even, for which

$$\begin{bmatrix}l & L' & L\\ 0 & 0 & 0\end{bmatrix}=(-1)^{J_s/2}\left[\frac{(J_s-2l)!(J_s-2L')!(J_s-2L)!}{(J_s+1)!}\right]^{1/2}\left[\frac{(\frac{1}{2}J_s)!}{(\frac{1}{2}J_s-l)!(\frac{1}{2}J_s-L')!(\frac{1}{2}J_s-L)!}\right]. \quad (52)$$

We can now rewrite (42) with the help of (43), (47), and (48) as

$$D=\left\langle F_1,F_2;F,F_z\left|\frac{1}{|\mathbf{r}_1-\mathbf{r}_2|}\right|F_1',F_2';F',F_z'\right\rangle$$
$$=\sum_{J_2,L_2,J_2',L_2'}C^*_{K_2,J_2,L_2}C_{K_2',J_2',L_2'}\sum_{J_1,L_1,J_1',L_1'}C^*_{K_1,J_1,L_1}C_{K_1',J_1',L_1'}\sum_{l=0}^{\infty}R_l(1,2,1',2')$$
$$\times\delta_{J_1,J_1'}\langle L_1\|l\|L_1'\rangle[(2F_1'+1)(2L_1+1)]^{1/2}W(lL_1'F_1J_1;L_1F_1')$$
$$\times\delta_{J_2,J_2'}\langle L_2\|l\|L_2'\rangle[(2F_2'+1)(2L_2+1)]^{1/2}W(lL_2'F_2J_2;L_2F_2')(-1)^{F_1+F_1'+F_2+F_2'}$$
$$\times\sum_{F_{1z},(F_{2z}=F_z-F_{1z})}\sum_{F_{1z}',(F_{2z}'=F_z'-F_{1z}')}\langle F_1,F_{1z};F_2,F_{2z}|F_1,F_2;F,F_z\rangle\langle F_1',F_{1z}';F_2'F_{2z}'|F_1',F_2';F',F_z'\rangle$$
$$\times\sum_{m=-l}^{l}(-1)^m\delta_{F_{1z},-m+F_{1z}'}\langle l,-m;F_1',F_{1z}'|l,F_1';F_1,F_{1z}\rangle$$
$$\times\delta_{F_{2z},m+F_{2z}'}\langle l,m;F_2',F_{2z}'|l,F_2';F_2,F_{2z}\rangle\ , \quad (53)$$

where we have used the fact that the $C_{K,J,L}$ coefficients and R_l are independent of all F_{iz} quantum numbers. We have also used the fact that l,L_1',L_2' are integral, and that J_1,J_2,F_1,F_2' are odd multiples of $\frac{1}{2}$. The last three summations in (53) above can be written in terms of a Racah coefficient,[10]

$$D=\left\langle F_1,F_2;F,F_z\left|\frac{1}{|\mathbf{r}_1-\mathbf{r}_2|}\right|F_1',F_2';F',F_z'\right\rangle$$
$$=\sum_{J_2,L_2,J_2',L_2'}C^*_{K_2,J_2,L_2}C_{K_2',J_2',L_2'}\sum_{J_1,L_1,J_1',L_1'}C^*_{K_1,J_1,L_1}C_{K_1',J_1',L_1'}\sum_{l=0}^{\infty}R_l(1,2,1',2')$$
$$\times\delta_{J_1,J_1'}\langle L_1\|l\|L_1'\rangle[(2F_1'+1)(2L_1+1)]^{1/2}W(lL_1'F_1J_1;L_1F_1')$$
$$\times\delta_{J_2,J_2'}\langle L_2\|l\|L_2'\rangle[(2F_2'+1)(2L_2+1)]^{1/2}W(lL_2'F_2J_2;L_2F_2')$$
$$\times\delta_{F_z,F_z'}\delta_{F,F'}(-1)^{F_1+F_2'-F}[(2F_1+1)(2F_2+1)]^{1/2}W(F_1'F_2'F_1F_2;Fl)\ . \quad (54)$$

Note that (54) requires that total angular momentum be conserved for Auger processes in a quantum dot, as we would

expect for an interaction which is scalar, the Coulomb potential, in a spherically symmetric system. This is to be contrasted to the situation in the bulk in which the total linear momentum must be conserved. The exchange (the second) term in the integral (5) above can be obtained from (54) by replacing the subscripts 1 by 2 and vice versa.

4. *Checking the matrix element*

Since we were unable to find detailed discussions in the literature on the Auger rate in a semiconductor quantum dot, we discuss here and in the InSb example below some of the ways in which we checked our numerics. In checking the matrix elements calculated from (54), we note that the coefficients C can be checked in the limit of small wave vectors with the expressions in Sec. IV A. The Racah coefficients were checked with[10,32] tabulated values and known expressions. (The relative sign of the different angular momenta recouplings have been crucial in atomic physics calculations.) The most difficult thing to check in (54) is the Slater integral because this integral cannot be evaluated in closed form for many values of L_i, l. One exception to this occurs when $L_i = l = 0$ for $i = 1, 2, 1', 2'$, where we found that

$$\int_0^R r_2^2 dr_2 \int_0^R r_1^2 dr_1 j_0(K_2 r_2) j_0(K_2' r_2) \frac{4\pi}{r_>} j_0(K_1 r_1) j_0(K_1' r_1)$$

$$= \frac{\pi}{2K_1 K_2 K_1' K_2'}$$

$$\times \left[\mathrm{Si}[(K_1+K_1'+K_2+K_2')R] \left(\frac{1}{K_1+K_1'} + \frac{1}{K_2+K_2'} \right) + \mathrm{Si}[(K_1+K_1'-K_2-K_2')R] \left(\frac{1}{K_1+K_1'} - \frac{1}{K_2+K_2'} \right) \right.$$

$$+ \mathrm{Si}[(K_1+K_1'+K_2-K_2')R] \left(\frac{-1}{K_1+K_1'} - \frac{1}{K_2-K_2'} \right) + \mathrm{Si}[(K_1+K_1'-K_2+K_2')R] \left(\frac{-1}{K_1+K_1'} + \frac{1}{K_2-K_2'} \right)$$

$$+ \mathrm{Si}[(K_1-K_1'+K_2-K_2')R] \left(\frac{1}{K_1-K_1'} + \frac{1}{K_2-K_2'} \right) + \mathrm{Si}[(K_1-K_1'-K_2+K_2')R] \left(\frac{1}{K_1-K_1'} - \frac{1}{K_2-K_2'} \right)$$

$$+ \mathrm{Si}[(K_1-K_1'+K_2+K_2')R] \left(\frac{-1}{K_1-K_1'} - \frac{1}{K_2+K_2'} \right)$$

$$\left. + \mathrm{Si}[(K_1-K_1'-K_2-K_2')R] \left(\frac{-1}{K_1-K_1'} + \frac{1}{K_2+K_2'} \right) \right], \tag{55}$$

where the $\mathrm{Si}(x) \equiv \int_0^x dt \sin t/t$ are[30] sine integrals, and the normalization integrals are

$$\int_0^R r'^2 dr' [j_0(kr')]^2 = \frac{R}{2k^2} \left[1 - \frac{\sin(2kR)}{(2kR)} \right]. \tag{56}$$

[As expected, the right-hand side of (55) is symmetric with respect to interchanging the labels $1, 1'$ with $2, 2'$, or interchanging primed with unprimed K_i. Also, both sides of (55) correctly approach $\frac{8}{15}\pi R^5$ for small R.] We found that our numerical evaluation of the Slater integral agreed to at least eight decimal places with the exact expression above; the errors seem to come from approximating $\mathrm{Si}(x)$ in the exact expression with products of sinusoids and rational polynomials, which are only accurate[30] to eight decimal places.

V. SAMPLE CALCULATION: ELIMINATING THE ROOM-TEMPERATURE AUGER RATE IN AN InSb QUANTUM DOT

In our example, we will assume there are two electrons in the conduction band and two holes in the valence band. The reason is that quantum-dot gain calculations indicate[8] that the threshold carrier density in the quantum dot for both holes and electrons is a few times 10^{18} cm^{-3}, which is equivalent to having a few electrons and holes in each quantum box with a typical dimension of 100 Å. We calculate the Auger rate by using (54), (35), and (37) in (34).

An example of a quantum dot in which large potential barriers can greatly reduce the Auger rate is an InSb quantum dot with CdTe barriers. InSb has[20] a room-temperature, bulk band gap of 163 meV, a spin-orbit splitting of 850 meV, a low-frequency dielectric of $17.7\epsilon_0$, light-hole, heavy-hole, and conduction-band effective masses at the Γ point of $0.015m_0$, $0.4m_0$, and $0.014m_0$, respectively. In our calculations, we do not include the temperature dependence of the above parameters in the bulk. The reason is that we want our calculated Auger rate temperature dependence to come only from the carrier statistics. Our calculated Auger lifetimes are thus expected to be most accurate near room temperature. CdTe has a room-temperature[13–15,20] bulk conduction-band edge which is 420 meV above that of InSb and a valence-band edge which is 850 meV below that of InSb. CdTe has heavy-hole and conduction-band effective masses of $0.35m_0$ and $0.11m_0$, respectively.

It is difficult to compare our results with anything in the literature since we were able to find only one Auger calculation for a quantum dot in the literature.[33] Howev-

er, that paper presented equations for the Auger rate which are valid in the bulk. We do not know if they actually derived an expression similar to (54) above. We also do not know if they used a basis of total-angular-momentum single-particle and multiparticle eigenstates; nor do we know if they included the band mixing resulting from using such a basis. In the following paragraphs, we discuss why our results should be considered plausible.

Table III shows the 19 conduction-band and the first 19 of the 448 valence-band single-particle bound states in a 150-Å-radius InSb quantum dot surrounded by CdTe barriers. All energies are measured from the valence-band maximum. The integer p designates which eigenstate, (25) or (26), was used in finding the bound states.

It is not practical to tabulate the $(19\times19/2)\times448$ possible entries that can go into a Grotrian diagram of all *CCCV* Auger processes, although they are available upon request. Figure 2 shows part of a Grotrian diagram for the *CCCV* Auger process in our InSb quantum dot. In labeling our Grotrian diagram, we will denote multiparticle states as $[n_1(L_1)_{F_1}n_2(L_2)_{F_2}]n_1'(L_1')_{F_1'}$, where it is understood that linear combinations of the products of the two single-particle states inside the square brackets above must be taken so that the two initial particles 1 and 2 form a state with definite angular momentum in accordance with (32) above. Similarly, it is understood that the two final particles 1′ and 2′ must form a state with definite angular momentum. Quantum numbers for the 2′ state are not given in this diagram because the Auger lifetimes given assume that we have summed over all possible 2′ states which can satisfy energy and angular-momentum conservation with the given 1, 2, and 1′ particles. The implicit assumption in this notation is that the microscopic (Bloch periodic) part of the wave functions in all conduction-band states have $J=\frac{1}{2}$, and all light- and heavy-hole valence-band states have $J=\frac{3}{2}$.

TABLE III. The 19 conduction-band and the first 19 of 448 valence-band single-particle bound states in a 150-Å-radius InSb quantum dot surrounded by CdTe barriers. All energies are measured from the valence-band maximum. The integer p designates which eigenstate, (25) or (26), was used in finding the bound states. The single-particle notation is $n(L)_F$, where n denotes the orbital, F is the single-particle total-angular-momentum quantum number, and where (L) is a letter $(S,P,D,\ldots)$ denoting the envelope angular momentum of the dominant portion of the wave function.

Level	Conduction-band state			Valence-band state		
number	Energy	p	State	Energy	p	State
1	244.25	0	$1S_{0.5}$	−13.70	0	$1S_{1.5}$
2	300.39	1	$1P_{0.5}$	−17.94	1	$1P_{1.5}$
3	300.39	0	$1P_{1.5}$	−20.35	0	$1P_{2.5}$
4	356.38	0	$1D_{2.5}$	−26.50	1	$1D_{2.5}$
5	356.38	1	$1D_{1.5}$	−27.99	0	$1D_{3.5}$
6	379.89	0	$2S_{0.5}$	−33.78	0	$2S_{1.5}$
7	412.18	0	$1F_{3.5}$	−35.39	1	$1F_{3.5}$
8	412.18	1	$1F_{2.5}$	−35.48	1	$2P_{1.5}$
9	446.39	1	$2P_{0.5}$	−36.64	0	$1F_{4.5}$
10	446.39	0	$2P_{1.5}$	−45.13	1	$1G_{4.5}$
11	467.80	1	$1G_{3.5}$	−45.17	0	$2P_{2.5}$
12	467.80	0	$1G_{4.5}$	−46.30	0	$1G_{5.5}$
13	510.90	0	$2D_{2.5}$	−52.80	1	$2D_{2.5}$
14	510.90	1	$2D_{1.5}$	−55.17	1	$3P_{1.5}$
15	523.31	0	$1H_{5.5}$	−55.82	1	$1H_{5.5}$
16	523.31	1	$1H_{4.5}$	−56.96	0	$1H_{6.5}$
17	526.60	0	$3S_{0.5}$	−57.25	0	$2D_{3.5}$
18	574.13	0	$2F_{3.5}$	−58.53	0	$3S_{1.5}$
19	574.13	1	$2F_{2.5}$	−67.31	1	$2F_{3.5}$

The long horizontal line in Fig. 2 indicates the energy of the CdTe conduction-band edge, above which E_2' must lie in order for the Auger process to be allowed. In the region below the long horizontal line are shown those states for which Auger processes are *not* energetically allowed because of the large potential barriers formed by CdTe. When the electrons 1 and 2 are in the initial states $[1S_{1/2}1S_{1/2}]$ or $[1S_{1/2}1P_{1/2}]$ or $[1S_{1/2}1P_{3/2}]$, the CdTe potential barriers prevent the first 32, the first 9, and the first 9 hole energies, respectively, to participate in an Auger process, as we indicate schematically. As a check of the diagram, note that all Auger rates are zero when $F_1=F_2$, as expected, because the direct term (54) is the same as the analogous exchange term when $F_1=F_2$. In quantum boxes, which are probably easier to fabricate than quantum spheres, total angular momentum would not be conserved in an Auger process, and many more of the energetically allowed states, which lie above the long horizontal line in the Grotrian diagram, would have finite Auger lifetimes. Thus, it becomes imperative that such quantum boxes be surrounded by large potential barriers in order to energetically exclude many possible Auger processes. The lifetimes given in the Grotrian diagram do not include the temperature-dependent occupation factors (35).

As one check of our results, we expect that Auger processes involving only lower-order multipole transitions to have smaller lifetimes than processes that involve higher-order multipole transitions. This is confirmed by the lifetimes given in our Grotrian diagram. The order of the transition is determined by the three Racah coefficients in (54) and the total single-particle (and multiparticle) angular momenta F_i that enter into that equation. We note that the *CCCV* Auger processes involving the states $[1S_{1/2}1P_{1/2}]2P_{5/2}$ (9.0 ns) or $[1S_{1/2}1P_{1/2}]2D_{5/2}$ (27.4 ns) have only $l=2,3$ in (54) and thus have shorter lifetimes than *CCCV* Auger processes involving $[1S_{1/2}1P_{1/2}]1G_{11/2}$ (81.1 ns) or $[1S_{1/2}1P_{1/2}]1H_{11/2}$ (277.0 ns), which have only $l=5,6$ in (54).

Using the temperature-dependent occupation factors (35) with the Grotrian diagram and summing all contributions to the Auger rate gives the Auger rate temperature dependences shown in Figs. 3 and 4. (The data presented in both figures are the same, but the axes are labeled differently.) In our calculations we included all terms for which (35) evaluated at 780 K is greater than 7×10^{-8} for *CCCV* processes and greater than 7×10^{-10} for *CVVV* processes. For the *CVVV* processes, we needed to include terms with very small occupation probabilities because those transitions which would have had much

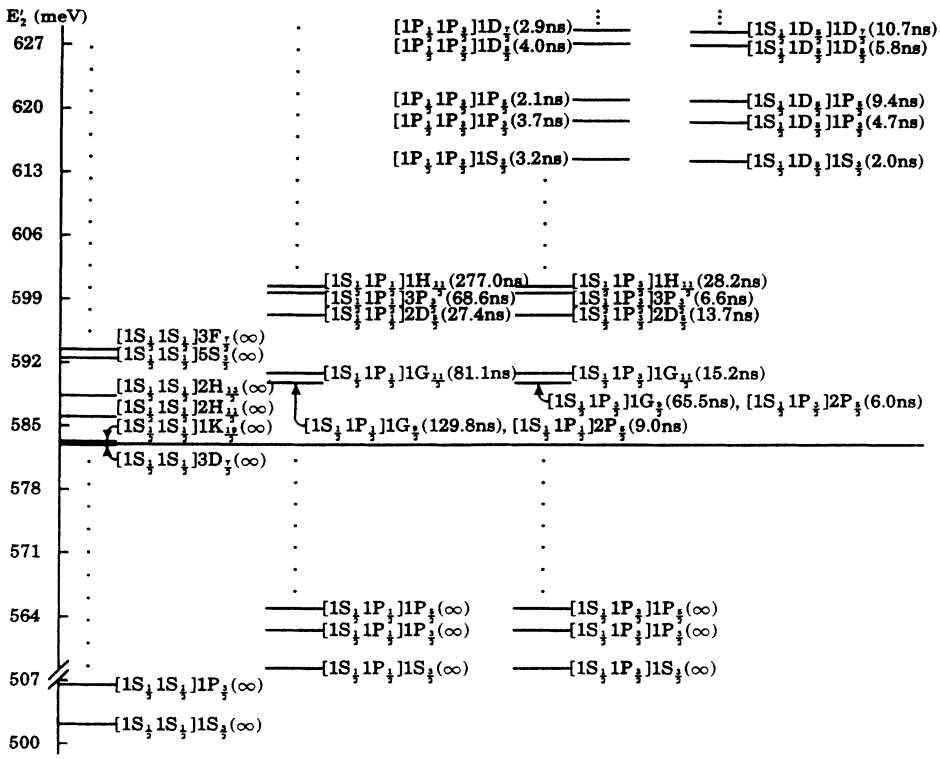

FIG. 2. Part of a Grotrian diagram for the *CCCV* Auger process in a 150-Å-radius InSb quantum dot surrounded by CdTe barriers. The ordinate is the final particle energy E_2' in meV. In the region below the long horizontal line are shown those states for which Auger processes are *not* allowed because of the large potential barriers formed by the CdTe. Multiparticle states are denoted as $[n_1(L_1)_{F_1} n_2(L_2)_{F_2}]n_1'(L_1')_{F_1'}$, where it is understood that linear combinations of the products of the two initial single-particle states, 1 and 2, inside the square brackets above must be taken so that they form a state with definite angular momentum. Similarly, the two final particles, 1′ and 2′, must form a state with definite angular momentum. All possible 2′ states which can satisfy energy and angular-momentum conservation with the given 1, 2, and 1′ particles have been summed over to obtain the given lifetimes. The lifetimes given in the Grotrian diagram do not include the temperature-dependent occupation factors (35).

larger occupation probabilities are not energetically allowed as a result of the large potential barriers formed by the CdTe. We chose these numbers so as to minimize our use of Cray time. We calculated some of the terms we did not include and estimate that our answers are accurate to about 5% at 780 K and much better than that at room temperature.

We see from Figs. 3 and 4 that the room-temperature Auger lifetime for this InSb quantum dot with a band gap at 4.8 μm (258 meV) is about 135 ns. This is to be compared with the calculated Auger rates for other semiconductors with band gaps in the infrared. For GaSb with a band gap of 670 meV (1.8 μm), the Auger lifetime at 77 K for a carrier concentration in the bulk of $2/(\frac{4}{3}\pi R^3)$ was calculated to be about[34] 0.01 ns and measured to be about to[34] 1 ns for our volume of $\frac{4}{3}\pi(150\ \text{Å})^3$. (These numbers are obtained from their formula for the Auger rate per unit volume $R_A = Cn^2p$, where C has calculated and measured values of 2.4×10^{-24} cm^{6}s^{-1} and 2.2×10^{-26} cm^{6}s^{-1}, respectively.) A 4.5-ns Auger lifetime[35] was found at liquid-nitrogen temperature for a conventional 10-μm $Pb_{0.82}Sn_{0.18}Te$ laser, whose active region injected carrier concentration is 0.8×10^{17} cm^{-3} for our volume of $\frac{4}{3}\pi(150\ \text{Å})^3$. (This number comes from their[35] value of 250 A cm^{-2} μm^{-1} of the Auger current per unit volume and agrees with their assessment of the Auger lifetime.) Room-temperature bulk InSb seems to have calculated Auger lifetimes between 0.1 and 1 ns, depending[36] on how the atomic orbitals and nonparabolic energy bands are calculated.

The Auger rate temperature dependence: the effect of carrier statistics

As a quick check of the temperature dependence obtained for the *CCCV* process, note that at low temperatures the Auger rate appears to vary as $\exp(-T_0/T)$, where T_0 can be measured from Fig. 3 to be about 660 K. This makes physical sense because at these very low temperatures the dominant contribution to the Auger rate comes from those energy levels lying closest to the InSb band gap but which have enough energy so that E_2' is a (continuum) state lying above the potential barriers. From the Grotrian diagram, we see that the dominant contribution to the Auger rate comes from the initial state with two of its electrons having energies $E_1 = 244.2$ meV and $E_2 = 300.4$ meV, and with one of its final-state electrons having energy $E_1' = -45.2$ meV, where we have

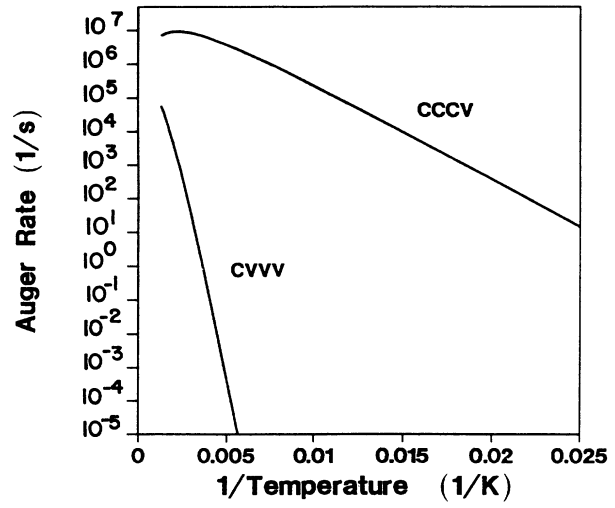

FIG. 3. The inverse temperature dependence of the *CCCV* and *CVVV* Auger rates for a 150-Å-radius InSb quantum dot surrounded by CdTe barriers. Two electrons and two holes are assumed to occupy each quantum dot. Note that the *CVVV* Auger rate is much smaller than the *CCCV* rate because the bulk potential barrier seen by the holes is much larger (850 meV) than that seen by the electrons (420 meV). The exponential dependence of the Auger rate on inverse temperature at low temperatures and departures from this dependence at higher temperatures is expected from the carrier statistics, as in (57).

calculated the conduction-band and valence-band Fermi energies to be at $E_{fc}=270.4$ meV and $E_{fv}=-13.1$ meV at $T=20$ K. Since the occupation factors must satisfy $f(E_1)=1$ and $f(E_2')\ll f(E_2), f(E_1')$ at these low temperatures, we expect the Auger rate to vary as

$$\exp\left[-\frac{E_2-E_{fc}}{k_BT}+\frac{E_1'-E_{fv}}{k_BT}\right]\equiv\exp\left[\frac{-T_0}{T}\right],$$

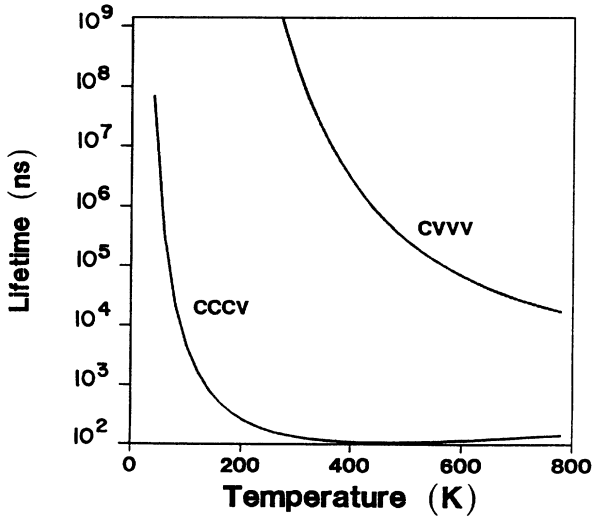

FIG. 4. The temperature dependence of the *CCCV* and *CVVV* Auger lifetimes for a 150-Å-radius InSb quantum dot surrounded by CdTe barriers. Note that the room-temperature Auger lifetime is about 135 ns.

where $T_0=720$ K in good agreement with the value obtained from Fig. 3. Of course, to get an accurate picture at very low temperatures, other loss mechanisms, such as phonon-assisted Auger processes, must be considered in addition to the *CCCV* and *CVVV* Auger processes discussed here.

Figure 3 shows that at low temperatures, the Auger rate has an exponential dependence on inverse temperature. At higher temperatures, the Auger rate deviates from this temperature dependence, reaches a peak around 450 K, and then becomes smaller at even higher temperatures. All of this can be understood from the carrier statistics. Recall that in the *bulk*, the Fermi-Dirac occupation probabilities in (35) can be approximated as Maxwellian in the nondegenerate limit,[1]

$$f_c(E)\simeq\frac{n}{N_c}\exp\left[\frac{-E}{k_BT}\right]\sim T^{-3/2}\exp\left[\frac{-E}{k_BT}\right],$$
$$f_v(E)\simeq\frac{p}{N_V}\exp\left[\frac{-E}{k_BT}\right]\sim T^{-3/2}\exp\left[\frac{-E}{k_BT}\right], \tag{57}$$

where

$$N_c=2\left[\frac{2\pi m_c k_BT}{\hbar^2}\right]^{3/2},$$
$$N_v=2\left[\frac{2\pi k_BT}{\hbar^2}\right]^{3/2}(m_{lh}^{3/2}+m_{hh}^{3/2}), \tag{58}$$

and where n,p are the electron and hole bulk populations. The $T^{-3/2}$ dependence simply expresses the fact that as the temperature is increased, E_{fc} becomes smaller and E_{fv} becomes larger in order to keep the total electron hole populations constant. Equation (57) comes from approximating the bulk expression for the total carrier concentration

$$n=N_c\frac{2}{\sqrt{\pi}}\int\frac{\epsilon^{1/2}d\epsilon}{1+\exp\left[\epsilon-\frac{E_{fc}}{k_BT}\right]},$$
$$p=N_v\frac{2}{\sqrt{\pi}}\int\frac{\epsilon^{1/2}d\epsilon}{1+\exp\left[\epsilon-\frac{E_{fv}}{k_BT}\right]}. \tag{59}$$

For a semiconductor quantum dot, the integrals in Eq. (59) becomes sums over discrete energies. However, Eq. (57) is still a good rough approximation (in the nondegenerate limit) in the sense that the total number of carriers with wave vector less than K_F can still be approximated by $(K_FL)^3/(3\pi^2)$, where L is between $\sqrt{2}R$ and $8R$, the length of a side of the inscribed and circumscribed cubes, respectively. Equation (57) shows the qualitative temperature dependence that we see in Figs. 3 and 4. (InSb melts[20] at 800 K, above which the Auger rate is not calculated.) Of course, one must remember that the Coulomb matrix element also has a weak temperature dependence.

Indeed, when (57) is used we obtain the following expression for the bulk *CCCV* Auger rate[34] per unit volume:

$$R_{A,\text{bulk}}=\left[\frac{32\beta|\langle u_1|u_1'\rangle\langle u_2|u_2'\rangle|^2}{(4\pi\epsilon)^2|\mathbf{K}_1-\mathbf{K}_1'|^4}\right]\times\left[\frac{\pi^{5/2}e^4}{\hbar}\right]\left[\frac{(E_T-E_g)^{1/2}}{(k_BT)^{3/2}}\right]\times\left[\frac{m_C(m_C+m_H)^2}{(2m_C+m_H)^3}\right]n^2p\times\exp\left[-\left[\frac{E_T-E_g}{k_BT}\right]\right], \tag{60}$$

where the threshold energy, defined as the minimum E_2' for which energy and momenta conservation can be satisfied in the bulk,[1] is measured form the band extremum,

$$E_T=E_2'=\frac{(m_1+m_2+m_1')E_g}{(m_1+m_2+m_1'-m_2')}, \tag{61}$$

where the masses are evaluated at each of the four energies, $1,2,1',2'$, where the overlap integrals and wave vectors are evaluated at threshold, and where β, a dimensionless number between 1 and 2, accounts for the exchange integral.[34]

The important thing is that we can now compare (61), the bulk threshold E_2', with the quantum dot "threshold" E_2',

$$E_{T,\text{ quantum dot}}=E_2'=V_{\text{barr},cb} \tag{62}$$

which in this case is 420 meV above the InSb conduction-band edge. Using the effective masses at the band extrema given above, the exponential in (60) at room temperature becomes $\exp(-0.213)$ in the bulk and $\exp(-9.930)$ in our quantum dot. This four-orders-of-magnitude difference between the bulk and quantum-dot Auger rates puts our calculated room-temperature lifetime of 135 ns in the right order of magnitude. We now see how the large potential barriers formed by the CdTe can greatly reduce the Auger rate as compared with the bulk.

It has been claimed[37] that in a quantum-dot laser, the carrier statistics are no longer important since the separation between the quantized energy levels can be made large compared to k_BT. However, in the numerical example above, the separation between the quantized energy levels was chosen to be small so that the quantum-dot zero-point confinement energies in the conduction and valence bands are small. We want small zero-point energies so that most of the electrons and holes are located near the band extrema. In this way, the large potential barriers surrounding the quantum dot can prevent energy conservation from being satisfied for many Auger processes. In other words, large zero-point energies would mean that the criterion (14) must be made more strict, and many of the materials listed in Table I would no longer provide suitably large potential barriers to greatly reduce the Auger rate. Thus, large zero-point energies are often undesirable for many of the barrier materials listed in Table I; and the carrier statistics in the quantum dots described in this example provide the exponential inverse temperature dependence at low temperatures and the cubic dependence on carrier concentration of the Auger rate, as was seen for bulk Auger rates.

Note that if the carrier and quantum-dot concentrations are chosen so that there is exactly one conduction-band electron and one valence-band hole per sphere, then there are *not enough carriers* to allow Auger processes to occur. One electron and one hole per quantum dot may not be enough carriers to produce gain in a quantum-box laser, since calculations seem to indicate[8] that each quantum dot needs a threshold of at least two electrons and holes. Also observe that linear momentum conservation is not required for Auger processes in quantum dots, as it had been for bulk Auger processes. As long as energy conservation is satisfied, Auger processes will occur as outlined in this paper. In this paper we have chosen the quantum dots to be surrounded by very large potential barriers, so as to make continuum energy states inaccessible for those Auger processes involving electrons and holes near the band extrema.

Observe also that should the energy of the final particle $2'$ occur just above the top of the energy barriers enclosing the quantum sphere, then the density of final states for particle $2'$ is vanishingly small. In practice, this observation may be difficult to utilize because the band lineup (in both the conduction and valence bands) in the barrier region is often a subject of debate for many materials.

VI. CONCLUSIONS

In this paper, we derive analytical expressions for the Auger rate in a quantum sphere in terms of Slater integrals, reduced matrix elements, and Racah coefficients. We show that, unlike the situation in the bulk, linear momentum conservation is not required for Auger processes in quantum dots. We note that total angular momentum must be conserved for the process, which is a consequence of the spherical symmetry of the problem. We use a basis of total-angular-momentum single-particle and multiparticle eigenstates. We show that the room-temperature Auger rate can be vastly reduced by surrounding the quantum dot with very large potential energy barriers, thus making continuum energy states unavailable as final states for many Auger processes. We discussed possible materials where the Auger rate is minimized and presented a practical example of this. We presented partial Auger rates in a Grotrian diagram. We calculated and discussed the temperature dependence of the quantum dot Auger rates. The Auger rates in a quantum sphere laser can be reduced by requiring quantum spheres of uniform size and shape to be constructed in carefully chosen materials.

ACKNOWLEDGMENTS

I am greatly indebted to P. L. Hagelstein for many fruitful discussions and much encouragement. I would also like to thank MIT Lincoln Laboratory for Cray time under Contract No. 00235. M. H. Chen was helpful in providing some reference papers.

APPENDIX A: BOUND-TO-BOUND PROCESSES IN QUANTUM DOTS AND THE CONFIGURATION INTERACTION IN ATOMS

We now show that bound-to-bound "Auger" processes are not Auger processes. We do so by first showing that quantum-dot bound-to-bound "Auger" process is analogous to what is termed configuration interaction[38–41] (CI) in atomic physics literature. Having done so, we show that the electron-electron interaction, allegedly responsible for the quantum-dot bound-to-bound "Auger" processes, will merely mix the quantum-dot multielectron bound eigenstates and lift some energy degeneracies. As in the atomic physics literature, we show how the CI is included in time-*independent* perturbation theory. Thus, the CI in atoms, as well as the bound-to-bound "Auger" processes in quantum dots, are part of the time-*independent* description of atoms and quantum dots. As such, the CI in quantum dots, as in atoms, is not an Auger process.

The electron-electron repulsion is responsible for both Auger processes and the CI. Thus, if we write the full Hamiltonian as

$$H_{\text{tot}}=H_0+H' \tag{A1}$$

where

$$H_0=\sum_{i=1}^{N}\left[\frac{p_i^2}{2m_i}+U(\mathbf{r}_i)\right] \tag{A2}$$

with N as the total number of electrons in the atom or quantum dot and $U(\mathbf{r}_i)$ as the potential energy seen by each electron [either the spherical square-well potential in the quantum dot or the nuclear attraction potential $Ze^2/(4\pi\epsilon r_i)$ in the atom], and with

$$H'=\sum_{i>j}\frac{e^2}{4\pi\epsilon r_{ij}} \tag{A3}$$

as the electron-electron repulsion energy, then we have presented the eigenstates of H_0 in our paper. The effects of (65) are what we now consider.

Without loss of generality, we consider quantum dot *CCCV* bound-to-bound "Auger" processes for now. In this case, we would have an electron in state 1 (a conduction-band bound state) making a nonradiative transition to the unoccupied bound state 1′ in the valence band, while another conduction-band electron (in bound state 2) is excited up to bound state 2′, also in the conduction band. In order to satisfy energy conservation, the energy E_i of the initial state, consisting of electrons 1,2, and the core electrons, must equal the energy E_f of the final state, consisting of electrons 1′,2′, and the core electrons. The CI of atomic physics considers the effects of (65) on the different (nearly degenerate) multielectron eigenstates of H_0. For example, Dyall and Larkins[38] have calculated the CI of $nsnp^6$, $ns^2np^4n's$, and $ns^2np^4n''d$, with n' between $n+1$ and $n+4$, and n'' between n and $n+3$ (except Ne) for $n=2$ (Ne), $n=3$ (Ar), $n=4$ (Kr), and $n=5$ (Xe). (These multielectron states are nearly degenerate in energy.) For Xe, we would have a CI (Refs. 38 and 39) between

$$5s^15p^6 \text{ and } 5s^25p^46s^1\ , \tag{A4}$$

among other states.

In both the quantum-dot and the atomic physics problem, there are two (sometimes more) multielectron states involved: One state has a hole and two (relatively) low-energy electrons, and the other has an electron replacing the hole and a (relatively) high-energy (excited) electron. (The nomenclature "hole" is also used in atomic physics.) To show that quantum-dot bound-to-bound "Auger" processes and atomic CI are analogous is just a matter of keeping track of the electrons involved. In both cases, the two relevant multielectron eigenstates of H_0 have the form

$$|i\rangle=a_1^\dagger a_2^\dagger|C\rangle \text{ and } |f\rangle=a_{1'}^\dagger a_{2'}^\dagger|C\rangle\ , \tag{A5}$$

where $a_i^\dagger$ is the creation operator for the bound electron $i, i=1,2,1',2'$, and $|C\rangle$ denotes the core electrons which do not make any transitions in the process. For the Xe example in (66), the labels 1,2 denote $5p$ electrons, and 1′,2′ denote $5s$, $6s$ electrons, respectively, so that

$$\begin{aligned}|i\rangle&=|[\text{Kr}]4d^{10}5s^15p^6\rangle\ ,\\ |f\rangle&=|[\text{Kr}]4d^{10}5s^25p^46s^1\rangle\ ,\\ |C\rangle&=|[\text{Kr}]4d^{10}5s^15p^4\rangle\ ,\end{aligned} \tag{A6}$$

where [Kr] denotes the electron configuration of ground-state Kr. For quantum-dot *CCCV* Auger processes, the labels 1,2 denote the initial electrons (*not* holes), and 1′,2′, the final electrons (*not* holes) in the bound-to-bound process, as described already in our paper, so that

$$\begin{aligned}|i\rangle&=|1,2,\text{ other } e^-s\rangle\ ,\\ |f\rangle&=|1',2',\text{ other } e^-s\rangle\ ,\\ |C\rangle&=|\text{ other } e^-s\rangle\ .\end{aligned} \tag{A7}$$

Observe that in both the quantum-dot and the Xe examples, none of the electrons in both $|i\rangle$ and $|f\rangle$ are continuum (unbound or free) electrons, as we are studying bound-to-bound processes.

Having shown that the quantum-dot bound-to-bound "Auger" problem is analogous to the CI in atomic physics, we use the atomic physics literature to show how (A3) affects the states (A5). In atomic physics, the CI[38–41] is calculated with (A3) as a time-independent perturbation. Denote the eigenvalues of H_0 associated with (A5) as E_i and E_f (which are nearly degenerate), respectively. For now, we assume that at this multielectron energy $E_i\simeq E_f$, only these two states will be strongly mixed by H'. (It is easy to include more states in this nearly degenerate time-independent perturbation[39] theory.) Time-independent perturbation theory approximates the eigenvectors of H_{tot} as

$$|\psi\pm\rangle=C_i|i\rangle+C_{f\pm}|f\rangle\ , \tag{A8}$$

where

$$\begin{bmatrix}E_i' & \langle i|H'|f\rangle\\ \langle f|H'|i\rangle & E_f'\end{bmatrix}\begin{bmatrix}C_i\\ C_f\end{bmatrix}=E\begin{bmatrix}C_i\\ C_f\end{bmatrix} \tag{A9}$$

with $E'_m = E_m + \langle m|H'|m\rangle$, $m = i,f$. Upon diagonalization of (A9), we have the eigenenergies

$$E_\pm = \left[\frac{E'_i+E'_f}{2}\right] \pm \left[\left[\frac{E'_i-E'_f}{2}\right]^2 + |\langle i|H'|f\rangle|^2\right]^{1/2}, \tag{A10}$$

and where, to within a normalization constant,

$$C_i = \langle i|H'|f\rangle , \tag{A11}$$

$$C_{f\pm} = \left[\frac{-E'_i+E'_f}{2}\right] \pm \left[\left[\frac{E'_i-E'_f}{2}\right]^2 + |\langle i|H'|f\rangle|^2\right]^{1/2} . \tag{A12}$$

Thus, the electron-electron interaction H' will mix the quantum-dot multielectron bound eigenstates according to (A8) and lift energy degeneracies according to (A10), as is the case for CI in atoms. As in the CI of the atomic physics literature, quantum-dot bound-to-bound "Auger" processes can be included in a time-*independent* description of the quantum dot, as discussed here. Such a time-*independent* description is *not* that of an Auger process.

APPENDIX B: THE PARAMETERS USED IN OUR k·p HAMILTONIAN

The modified Luttinger parameters are

$$\gamma_1 = \gamma_1^{\text{true}} - \frac{2P^2}{2(E_c - E_v)} , \tag{B1}$$

$$\gamma_2 = \gamma_2^{\text{true}} - \frac{P^2}{3(E_c - E_v)} . \tag{B2}$$

The Luttinger parameters are chosen so that the hole effective masses, m_{hh}, m_{lh}, at zero wave vector are their experimental values,

$$\gamma_1^{\text{true}} - 2\gamma_2^{\text{true}} = \frac{\hbar^2}{m_{\text{hh}}} , \tag{B3}$$

$$\gamma_1^{\text{true}} + 2\gamma_2^{\text{true}} = \frac{\hbar^2}{m_{\text{lh}}} . \tag{B4}$$

The Kane momentum matrix element is chosen to match the experimental conduction-band effective mass m_c at zero wave vector

$$\frac{\hbar^2}{m_c} = \frac{\hbar^2}{m_0} + \frac{4P^2}{3E_g} + \frac{2P^2}{3(E_g+\Delta)} , \tag{B5}$$

where m_0 is the free electron mass and E_g is the band gap. Thus, we set

$$\gamma_1^{\text{true}} = \frac{\hbar^2}{2m_0}\left[\frac{1}{m_{\text{lh}}/m_0} + \frac{1}{m_{\text{hh}}/m_0}\right] , \tag{B6}$$

$$\gamma_2^{\text{true}} = \frac{\hbar^2}{4m_0}\left[\frac{1}{m_{\text{lh}}/m_0} - \frac{1}{m_{\text{hh}}/m_0}\right] \tag{B7}$$

and

$$P^2 = \left[\frac{\hbar^2}{2m_0}\right]\left[\frac{1}{m_c/m_0} - 1\right]\left[\frac{E_g(E_g+\Delta)}{(E_g+\frac{2}{3}\Delta)}\right] . \tag{B8}$$

In real semiconductors, it is known that slightly different numerical values of the Kane momentum matrix element[42] are needed for each hole and conduction band, in order to match experimental values.

APPENDIX C: EVALUATING COULOMB INTEGRALS BY SOLVING A DIFFERENTIAL EQUATION

Integrals of the form

$$V(\mathbf{r}) = \int \frac{\rho(\mathbf{r}')d^3\mathbf{r}'}{|\mathbf{r}-\mathbf{r}'|} \tag{C1}$$

can be evaluated by noticing that[43]

$$\nabla^2 V = -4\pi\rho . \tag{C2}$$

Thus, if we write

$$\rho(\mathbf{r}) = \sum_{l,m} \rho_{lm}(r) Y_{lm}(\Omega) \tag{C3}$$

so that

$$\rho_{lm}(r) = \int d\Omega\, Y^*_{lm}(\Omega)\rho(\mathbf{r}) , \tag{C4}$$

then (C2) has the solution

$$V(\mathbf{r}) = \sum_{l,m} V_{lm}(r) Y_{lm}(\Omega) , \tag{C5}$$

with each term solving

$$\left[\frac{d^2}{dr^2} - \frac{l(l+1)}{r^2}\right][rV_{lm}(r)] = -4\pi[r\rho_{lm}(r)] . \tag{C6}$$

Invoking (39), the solution of (C6) is

$$V_{lm}(r) = \int_0^\infty r'^2 dr' \rho_{lm}(r')\left[\frac{4\pi}{2l+1}\right]\frac{r_<^l}{r_>^{l+1}} . \tag{C7}$$

Instead of evaluating (C7), we solve (C6) numerically, as discussed below.

Numerical solution of second-order ordinary differential equations

Most second-order ordinary differential equations can be written, possibly with a change of variables, as a second-order ordinary differential equation *with no first derivative term*. An equation of the form

$$y''(r) + F(r)y(r) = G(r) \tag{C8}$$

can be solved numerically with the Noumerov or royal road method, which is accurate to sixth order in the grid spacing $h = x_{n+1} - x_n$,

$$\left[1+\frac{h^2}{12}F_{n-1}\right]y_{n-1}+[-(2-\tfrac{10}{12}h^2F_n)]y_n + \left[1+\frac{h^2}{12}F_{n+1}\right]y_{n+1} = \frac{h^2}{12}(G_{n-1}+10G_n+G_{n+1}) , \quad \text{(C9)}$$

where $F_m=F(r_m)$, $y_m=y(r_m)$, and $G_m=G(r_m)$. The tridiagonal matrix equation (C9) can be solved in an efficient and stable manner by using Gaussian elimination with partial pivoting.

In generating (modified or ordinary) spherical Bessel functions or in solving Poisson's equation, we want numerical solutions of the equation

$$y''(r)+\left[C-\frac{l(l+1)}{r^2}\right]y(r)=s(r) , \quad \text{(C10)}$$

where $C=\pm k^2$ and $s(r)=0$ for the ordinary and modified spherical Bessel functions $y(r)=rj_l(kr)$, respectively; and where $C=0$ and $s(r)=-4\pi r\rho_{lm}(r)$ for solutions $y(r)=r\tilde{V}_l(r)$ of Poisson's equation. Given values of F_m, G_m, and initial values y_0, y_1, iterative substitution in (C9) will yield *accumulated* errors in y_m that are[44,45] fourth order when F_m is non-negative, and, possibly, exponentially large when F_m is negative. This is much worse than the sixth-order error which limits this method. The reason is that the difference equation (C9) has two natural solutions, and the error in the initial conditions allows an "unwanted" solution (sinusoidal for F_m non-negative and exponential for F_m negative) to be picked up. To avoid this problem, we solve the set of equations (C9) as one matrix equation with boundary conditions at r_0, r_N. The boundary conditions used were easy to derive analytically; the singularity at $F(r=0)$ can be avoided by considering $F(r)y(r)$ together as $r\to 0$. For spherical Bessel functions generated in this way,

$$\lim_{r\to 0}F_n(r)[rj_n(kr)]=\begin{cases}-\frac{2}{3}|k| & \text{for } n=1\\ 0 & \text{for } n=0 \text{ or } n\geq 2 .\end{cases} \quad \text{(C11)}$$

For the solutions (C7) of Poisson's equation,

$$\lim_{r\to 0}\tilde{V}_l(r)=0 , \quad \text{(C12)}$$

$$\lim_{r\to 0}F_l(r)[r\tilde{V}_l(r)]=\begin{cases}(-2)\left[\frac{4\pi}{2l+1}\right]\int_0^\infty dr'\rho_{lm}(r') & \text{for } l=1\\ 0 & \text{for } l=0 \text{ or } l\geq 2 .\end{cases} \quad \text{(C13)}$$

If $\rho_{lm}(r')=0$ for $r'>R$, then solutions (C7) of Poisson's equation satisfy

$$\lim_{r\to R}r\tilde{V}_l(r)=\left[\frac{4\pi}{2l+1}\right]\left[\frac{1}{R^l}\right]\int_0^R dr'r'^{l+2}\rho_{lm}(r') . \quad \text{(C14)}$$

The Noumerov method usually requires equally spaced grid points. Since it is often desirable to make more function evaluations in regions where certain terms are rapidly varying, as in the case of the r^{-2} term for small r in the equation above, the equally spaced grid points may not be desirable. In such cases, a change of variables

$$\zeta=\zeta(r) \quad \text{(C15)}$$

can be made so that rapidly varying terms are sufficiently sampled. If we also define

$$\bar{y}(\zeta)=\left[\frac{d\zeta}{dr}\right]^{1/2}y(r) \quad \text{(C16)}$$

then (C10) can be written as

$$\frac{d^2\bar{y}}{d\zeta^2}+\left\{\left[\frac{3}{4}\left[\frac{d\zeta}{dr}\right]^{-1}\left[\frac{d^2\zeta}{dr^2}\right]^2-\frac{1}{2}\left[\frac{d^3\zeta}{dr^3}\right]\right]\left[\frac{d\zeta}{dr}\right]^{-3}+\left[C-\frac{l(l+1)}{r^2}\right]\left[\frac{d\zeta}{dr}\right]^{-2}\right\}\bar{y}(\zeta)=\left[\frac{d\zeta}{dr}\right]^{-2}\bar{s}(\zeta) \quad \text{(C17)}$$

for which the Noumerov method can be used. One possible change of variables, which is good for the r^2 terms, is

$$\zeta=\alpha r+\beta\ln r \quad \text{(C18)}$$

and

$$\bar{y}(\zeta)=\left[\alpha+\frac{\beta}{r}\right]^{1/2}y(r) \quad \text{(C19)}$$

for which (C10) becomes

$$\frac{d^2\bar{y}}{d\zeta^2}+\left[\left[\frac{-\beta}{r^3}\right]\left[\alpha+\frac{\beta}{r}\right]^{-4}\left[\alpha+\frac{\beta}{4r}\right]+\left[C-\frac{l(l+1)}{r^2}\right]\left[\alpha+\frac{\beta}{r}\right]^{-2}\right]\bar{y}(\zeta)=\left[\alpha+\frac{\beta}{r}\right]^{-2}\bar{s}(\zeta)\ . \tag{C20}$$

For our quantum-dot Bessel functions, this change of variables was not needed. However, the effect of the screened Coulomb potential of the nucleus on the different electron shells in an atom often necessitates such a change of variables.

[1]G. P. Agrawal and N. K. Dutta, *Long Wavelength Semiconductor Lasers* (Van Nostrand Reinhold, New York, 1986).

[2]A. Haug, *Theoretical Solid State Physics* (Pergamon, New York, 1972).

[3]A. Sa'ar and A. Katzir, in *Infrared Fiber Optics,* edited by J. A. Harrington and A. Katzir [Proc. SPIE **1048**, 24 (1989)].

[4]J. A. Harrington, *Infrared Fibers (0.8–12 μm)* [Proc. Soc. Photo-Opt. Instrum. Eng. **266**, 10 (1981)].

[5]T. Katsuyama and H. Matsumara, Appl. Phys. Lett. **49**, 22 (1986).

[6]K. Nassau and M. E. Lines, Opt. Eng. **25**, 602 (1986).

[7]A. I. Ekimov and Al. L. Efros, Acta Phys. Pol. A **79**, 5 (1991).

[8]M. Asada, Y. Miyamoto, and Y. Suematsu, IEEE J. Quantum Electron. **QE-22**, 1915 (1986).

[9]A. R. Beattie and P. T. Landsberg, Proc. R. Soc. London Ser. A **219**, 16 (1959).

[10]M. Tinkham, *Group Theory and Quantum Mechanics* (McGraw-Hill, New York, 1964).

[11]U. Fano, Phys. Rev. **140**, A67 (1965).

[12]J. C. Slater and G. F. Koster, Phys. Rev. **94**, 1498 (1954).

[13]G. Margaritondo and P. Perfetti, in *Heterojunction Band Discontinuities: Physics and Device Applications,* edited by F. Capasso and G. Margaritondo (Elsevier, New York, 1987).

[14]J. Tersoff, in *Heterojunction Band Discontinuities: Physics and Device Applications* (Ref. 13).

[15]A. D. Katnani, in *Heterojunction Band Discontinuities: Physics and Device Applications* (Ref. 13).

[16]*Molecular Beam Epitaxy and Heterostructures,* edited by L. L. Chang and K. Ploog (Martinus Nijhoff, Boston, 1985).

[17]C. Hsu, T. M. Duc, and J. P. Faurie, J. Vac. Sci. Technol. B **5**, 1229 (1987).

[18]C. G. Van de Walle and R. M. Martin, J. Vac. Sci. Technol. B **5**, 1225 (1987).

[19]K. J. Mackey, D. R. T. Zahn, P. M. G. Allen, R. H. Williams, W. Richter, and R. S. Williams, J. Vac. Sci. Technol. B **5**, 1233 (1987).

[20]*Handbook of Chemistry and Physics,* edited R. C. Weast (CRC, Boca Raton, FL, 1989).

[21]*Numerical Data and Functional Relationships in Science and Technology,* edited by R. H. Hellwege, Landolt-Börnstein, New Series, Vol. 17b (Springer-Verlag, New York, 1982).

[22]T. Dietl and J. Kossut, Phys. Rev. B **38**, 941 (1988).

[23]P. C. Sercel and K. J. Vahala, Phys. Rev. B **42**, 3690 (1990).

[24]M. G. Burt, S. Brand, C. Smith, and R. A. Abram, J. Phys. C **17**, 6385 (1984).

[25]G. C. Osbourn and D. L. Smith, Phys. Rev. B. **19**, 2124 (1979).

[26]V. Heine, Proc. Phys. Soc. London **81**, 300 (1963).

[27]M. Sweeny and J. Xu, Solid State Commun. **72**, 301 (1989).

[28]P. G. Burke, Comput. Phys. Commun. **1**, 241 (1970).

[29]G. Racah, Phys. Rev. **63**, 367 (1943).

[30]M. Abramowitz and I. A. Stegun, *Handbook of Mathematical Functions with Formulas, Graphs, and Mathematical Tables* (U.S. GPO, Washington, D.C., 1964).

[31]M. G. Burt, J. Phys. C **14**, 3269 (1981).

[32]M. Rotenberg, R. Bivins, N. Metropolis, and J. K. Wooten, Jr., *The 3-j and 6-j Symbols* (Technology, Cambridge, MA, 1959).

[33]R. A. Abram, R. W. Kelsall, and R. I. Taylor, J. Phys. Chem. Solids **49**, 607 (1988).

[34]A. Haug, D. Kerkhoff, and W. Lochmann, Phys. Status Solidi B **89**, 357 (1978).

[35]R. Rosman and A. Katzir, IEEE J. Quantum Electron. **QE-18**, 814 (1982).

[36]H. Bruhns and H. Kruse, Phys. Status Solidi B **97**, 125 (1980).

[37]K. J. Vahala, IEEE J. Quantum Electron. **QE-24**, 523 (1988).

[38]K. G. Dyall and F. P. Larkins, J. Phys. B **15**, 203 (1982).

[39]H. Smid and J. E. Hansen, J. Phys. B **16**, 3339 (1983).

[40]J. W. Cooper, U. Fano, and F. Prats, Phys. Rev. Lett. **10**, 518 (1963).

[41]J. D. Garcia and J. E. Mack, Phys. Rev. **138**, A987 (1965).

[42]J. S. Blakemore, J. Appl. Phys. **53**, R123 (1982).

[43]C. Froese Fischer, *The Hartree Fock Method for Atoms* (Wiley, New York, 1977).

[44]I. H. Sloan, J. Comput. Phys. **2**, 414 (1968).

[45]Z. Kopal, *Numerical Analysis* (Chapman and Hall, London, 1955).